IYQ Collection | Featured in Physics

Ultracold LiCr: A New Pathway to Quantum Gases of Paramagnetic Polar Molecules

S. Finelli,[1,2,3] A. Ciamei,[2,3,*] B. Restivo,[2,3] M. Schemmer,[2,3] A. Cosco,[1] M. Inguscio,[3,4] A. Trenkwalder,[2,3] K. Zaremba-Kopczyk,[5] M. Gronowski,[5] M. Tomza,[5,†] and M. Zaccanti[2,3]

[1] *Dipartimento di Fisica e Astronomia, Università di Firenze, Sesto Fiorentino 50019, Italy*
[2] *Istituto Nazionale di Ottica del Consiglio Nazionale delle Ricerche (CNR-INO), Sesto Fiorentino 50019, Italy*
[3] *European Laboratory for Non-Linear Spectroscopy (LENS), Università di Firenze, Sesto Fiorentino 50019, Italy*
[4] *Department of Engineering, Campus Bio-Medico University of Rome, Rome 00128, Italy*
[5] *Faculty of Physics, University of Warsaw, Pasteura 5, Warsaw 02-093, Poland*

(Received 9 February 2024; accepted 25 April 2024; published 12 June 2024)

Quantum gases of doubly polar molecules represent appealing frameworks for a variety of cross-disciplinary applications, encompassing quantum simulation and computation, controlled quantum chemistry, and precision measurements. Through a joint experimental and theoretical study, here we explore a novel class of ultracold paramagnetic polar molecules combining lithium alkali and chromium transition metal elements. Focusing on the specific bosonic isotopologue ^{6}Li^{53}Cr, leveraging on the Fermi statistics of the parent atomic mixture and on suitable Feshbach resonances recently discovered, we produce up to 50×10^3 ultracold LiCr molecules at peak phase-space densities exceeding 0.1, prepared within the least bound rotationless level of the LiCr electronic *sextet* ground state $X\,^6\Sigma^+$. By also developing new probing methods, we thoroughly characterize the molecular gas, demonstrating the paramagnetic nature of LiCr dimers and the precise control of their quantum state. We investigate their stability against inelastic processes and identify a parameter region where pure LiCr samples exhibit lifetimes exceeding 0.2 s. Parallel to this, we employ state-of-the-art quantum chemical calculations to accurately predict the properties of LiCr ground and excited electronic states. This *ab initio* model, able to reproduce the experimental Li-Cr high-spin, *octet* scattering length, allows us to identify both efficient paths to coherently transfer weakly bound LiCr dimers to their absolute ground state, and suitable transitions for their subsequent optical manipulation. Our studies establish Li-Cr as a prime candidate to realize ultracold gases of doubly polar molecules with significant electric (3.3 D) and magnetic ($5\mu_B$) dipole moments.

DOI: 10.1103/PRXQuantum.5.020358

I. INTRODUCTION

Ultracold gases of ground-state molecules with permanent electric dipole moments offer unprecedented opportunities to investigate quantum chemistry and many-body physics [1–3]. Recently, doubly polar molecules, possessing both an electric and a magnetic dipole moment, have attracted great attention, as they could offer even richer prospects: while the electric dipole gives rise to the long-range anisotropic interactions, the magnetic dipole arising from a nonzero electronic spin provides an additional degree of tunability in the system. A high phase-space density gas of such molecules will open up new venues in the context of quantum simulation [4–7] and computation [8,9], as well as quantum controlled chemistry [10]. This is exemplified by the pioneering work on excited-state NaLi dimers [11], which, despite featuring weak electric and magnetic dipole moments, provided new insights into ultracold reactive collisions [10,12].

Despite tremendous progress in the field [13], realization of degenerate gases of doubly polar ground-state molecules remains an unsurpassed challenge. While direct laser cooling schemes have been successfully applied to doubly polar radicals [14], the only experimental realizations of quantum degenerate molecular gases [15–17] exploit ultracold atomic mixtures, where atom pairs are first converted into weakly bound molecules across a Feshbach resonance (FR) [18] and later transferred to the absolute molecular ground state via stimulated Raman adiabatic passage (STIRAP). However, this two-step

*Corresponding author: ciamei@lens.unifi.it
†Corresponding author: michal.tomza@fuw.edu.pl

method has only been demonstrated on bialkali systems, whose ground state has zero electronic spin, and thus negligible magnetic moment. Binding alkali species with closed-shell atoms, which would endow ground-state molecules with the additional spin and magnetic moment, are currently under investigation, following the experimental discovery of FRs in alkali–alkaline-earth systems [19–21]. Yet, the extremely narrow character of available FRs, despite impressive technical effort [22], has so far hindered the first association step. Another proposed pathway to realize paramagnetic ground-state molecules relies on binding highly magnetic lanthanides with either alkali or closed-shell elements [23], and association of ultracold KDy Feshbach dimers has indeed been recently demonstrated [24]. Nonetheless, STIRAP transfer of such molecules to their ground state appears a formidable challenge, owing to the lack of spectroscopic data combined with the complex electronic configuration of these elements, which makes *ab initio* methods poorly reliable, if not unapplicable.

Here, through a joint experimental and theoretical study, we explore an alternative route towards ultracold doubly polar molecules by binding an alkali atom (A) with transition-metal chromium (Cr). The interaction between A ($^2S_{1/2}$) and Cr ($^7S_3$) has only weak magnetic anisotropy and leads to two spin multiplicities, similarly to standard bialkali systems. While the latter feature a singlet $X\,^1\Sigma^+$ ground and a triplet $a\,^3\Sigma^+$ first excited state [18], ACr systems exhibit a sextet $X\,^6\Sigma^+$ and an octet $a\,^8\Sigma^+$ symmetry; see Fig. 1(a) for the LiCr case. In its ground state ACr is thus expected to combine a high electronic spin with a strong $A^{\delta+}Cr^{\delta-}$ dipolar character [25]. Most importantly, the existence of two multiplicities, combined with the isotropic van der Waals interactions, makes the creation of ACr experimentally feasible with current technology. On the one hand, it leads to nonchaotic, bialkalilike FR spectra, well suited for molecule association. On the other hand, it allows for cutting-edge molecular structure calculations with predictive power over ground and lowest-lying electronic states. The ACr systems thus emerge as a unique playground that allows us to both produce loosely bound paramagnetic Feshbach dimers and subsequently transfer them to their absolute ground state, leveraging on the ultracold atom toolbox developed for bialkalis. This provides a bridge between the well-known bialkali dimers and more complex molecular species.

While early attempts focused on the rubidium-chromium mixture [26,27], we here explore the lithium-chromium system, and in particular the $^6Li^{53}Cr$ isotopologue, that combines the sole two stable fermionic isotopes of Li and Cr into bosonic dimers. This specific choice is motivated by the fact that Li-Cr Fermi mixtures have recently been realized [28], and that a suitable set of interspecies FRs has been identified [29]; see Fig. 1(b). Benefiting from a favorable good-to-bad collision ratio connected with the Fermi statistics of our atomic mixture, we experimentally demonstrate the efficient production of ultracold samples of up to 50×10^3 paramagnetic LiCr Feshbach dimers, at phase-space densities (PSDs) exceeding 0.1 and temperatures of about 200 nK. We exploit two interspecies s-wave FRs [see Fig. 1(b)] to access, with full internal quantum state control, the least bound rotationless vibrational level of the LiCr sextet ground state. This is confirmed by accurate measurements, also based on new all-optical probing methods, of the dimer magnetic moment and of the associated open-channel fraction, both found in remarkable agreement with theoretical expectations. Additionally, investigation of the collisional stability of the LiCr dimers as a function of the magnetic field detuning from the resonance pole allows us to identify a parameter region in which the molecular Bose gas can exhibit lifetimes exceeding 0.2 s, thanks to Pauli suppression of inelastic losses enabled by the fermionic nature of our mixture constituents [30,31]. Parallel to this, we perform state-of-the-art *ab initio* calculations to gain reliable predictions for both ground and excited electronic states of LiCr. Our *ab initio* model, that remarkably reproduces our experimental value of the Li-Cr *octet* scattering length recently determined [29], foresees for the sextet (octet) ground state a significant electric dipole moment of 3.3 D (0.7 D) that adds to the sizable magnetic one of $5\mu_B$ ($7\mu_B$). By inspecting the calculated electronic level structure, we identify the $(4)\,^6\Sigma^+$ as the best-suited intermediate electronically excited state to implement efficient STIRAP transfer to the LiCr sextet ground state. Moreover, we find that transitions to the $(2)\,^6\Pi$ excited state can be exploited for subsequent optical manipulation of LiCr molecules, including their direct imaging and, possibly, even the implementation of laser cooling schemes.

The paper is organized as follows. In Sec. II we summarize the experimental strategies to produce ultracold LiCr molecules and the properties of the parent atomic mixture under resonantly interacting conditions. In Sec. III we investigate the magnetoassociation process, including two-body adiabaticity, atom-to-molecule conversion efficiency, and the creation of a high phase-space density gas of LiCr. In Sec. IV we study single-particle properties of the newly formed Feshbach dimers, including their magnetic dipole moment and their binding energy, which we measure via a novel optical method. In Sec. V we identify and characterize the different loss mechanisms that limit the molecule lifetime and we show that, under optimal conditions, pure LiCr samples exhibit lifetimes exceeding 0.2 s. In Sec. VI, we present high-precision *ab initio* potential energy curves (PECs) for LiCr, we demonstrate their predictive power on the atomic scattering properties, and we then exploit them to unveil the doubly polar character of their absolute ground state. In Sec. VII, we employ our model to explore electronically excited states of LiCr, and identify an efficient STIRAP path connecting the last vibrational sextet

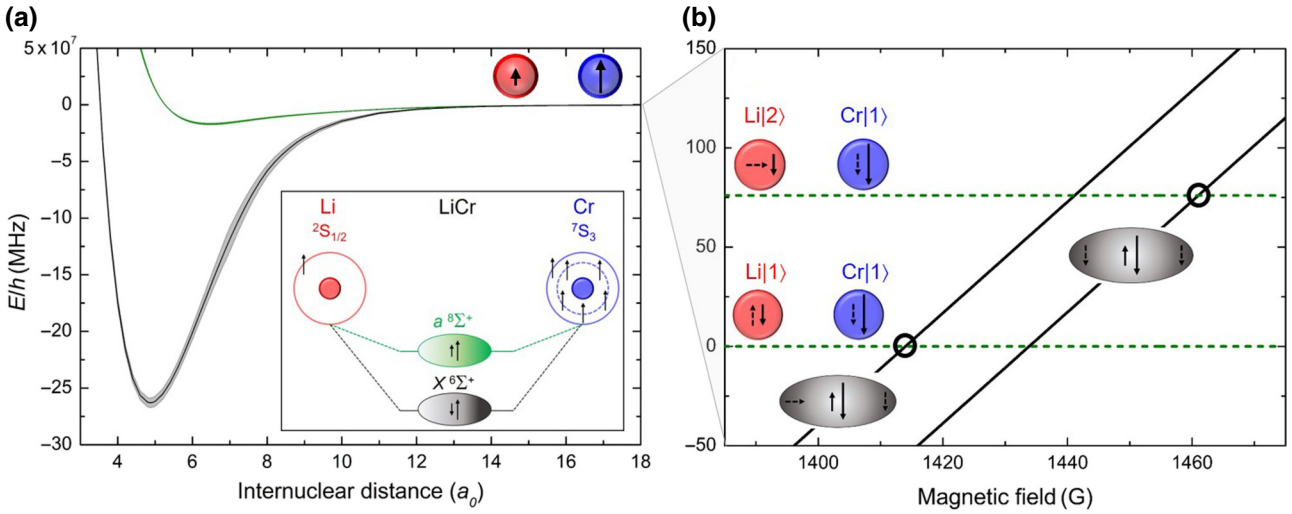

FIG. 1. Doubly polar LiCr dimers. (a) *Ab initio* potential energy curves for the $X\,^6\Sigma^+$ ground state and the $a\,^8\Sigma^+$ first excited state in Hund's case (a) representation. The inset shows a pictorial representation of the valence electrons for Li and Cr, and the resulting sextet and octet molecules with nonzero electronic spin and polarized charge density. (b) Energy of the atom pairs in the Li|1⟩-Cr|1⟩ and Li|2⟩-Cr|1⟩ channels, of pure octet character (dashed green lines), and of the molecular sextet levels (solid black lines) inducing the FRs used in this work (circled). Atomic Zeeman levels are labeled in order of increasing energy. Solid and dashed arrows indicate electronic and nuclear spins, respectively.

level to the absolute ground state. Finally, in Sec. VIII we provide a conclusion and an outlook on future research directions.

II. RESONANTLY INTERACTING Li-Cr FERMI MIXTURES AND EXPERIMENTAL PROCEDURES

The starting point of all our experiments is a weakly interacting, spin-polarized Fermi mixture of ^{6}Li and ^{53}Cr atoms produced through an all-optical protocol, detailed in Ref. [28], within a bichromatic optical dipole trap (BODT). The latter is realized by two overlapped infrared (IR) and green laser beams, propagating in the horizontal plane along the x direction, and it allows us to adjust the radial confinement of the two components almost independently, owing to the different Li and Cr polarizabilities to the two BODT lights [28]. The gravitational sag between the two clouds is compensated upon application of a weak, vertically oriented magnetic field gradient $\partial_z B$ of about 1.5 G/cm. The axial confinement is provided by the curvature of our magnetic field coils, employed to generate bias fields of up to 1.5 kG, and yielding a trapping potential along x 6 times tighter for chromium than for lithium; see the sketch in Fig. 2(a). Although the atom number, temperature, and degree of degeneracy of the two species can be widely tuned by adjusting the (absolute and relative) power of the two BODT beams [28], our experiments typically start with a Fermi gas of about 1.5×10^5 Li atoms at $T/T_F = 0.25$ with $T = 130(20)$ nK coexisting with a moderately degenerate sample of 0.8×10^5 Cr atoms at $T/T_F \simeq 0.5$ and $T = 220$ nK, with peak densities of about 10^{12} cm^{-3} for both components (here T_F denotes the Fermi temperature of a harmonically trapped Fermi gas).

Resonant tuning of the Li-Cr interaction, as well as magnetoassociation of atom pairs into LiCr dimers via magnetic field sweeps, are enabled by the presence of several interspecies FRs that we recently identified; see Ref. [29]. In particular, we focus on two specific s-wave FRs that occur in the Li|1⟩-Cr|1⟩ and Li|2⟩-Cr|1⟩ scattering channels (Zeeman levels are labeled in order of increasing energy), located at high fields around 1414 and 1461 G, respectively; see Fig. 1(b). Our choice is motivated by the fact that these two features exhibit the largest magnetic field width $\Delta B \sim 0.48$ G available in our mixture, combined with zero or negligible two-body loss rates. Most importantly for the present study, these FRs are induced by hyperfine coupling with the least bound, rotationless vibrational level of the $X\,^6\Sigma^+$ ground-state Born-Oppenheimer potential; see Fig. 1. As such, association of such *sextet* dimers represents an excellent starting point to subsequently implement efficient STIRAP transfer to the absolute ground state. However, in light of the high-field location of the selected FRs and of their narrow nature, as a crucial, preliminary step towards ultracold LiCr dimers, we first characterize the parent atomic mixture in the resonantly interacting, quantum degenerate regime, going beyond our previous work [29]. In particular, exploiting our improved control over magnetic fields in the setup (details in Appendix B), we accurately locate the FR pole, across which we extract both the elastic and inelastic collision rates per minority Cr atom, denoted $\gamma_{\rm el}$ and $\gamma_{\rm loss}$, respectively.

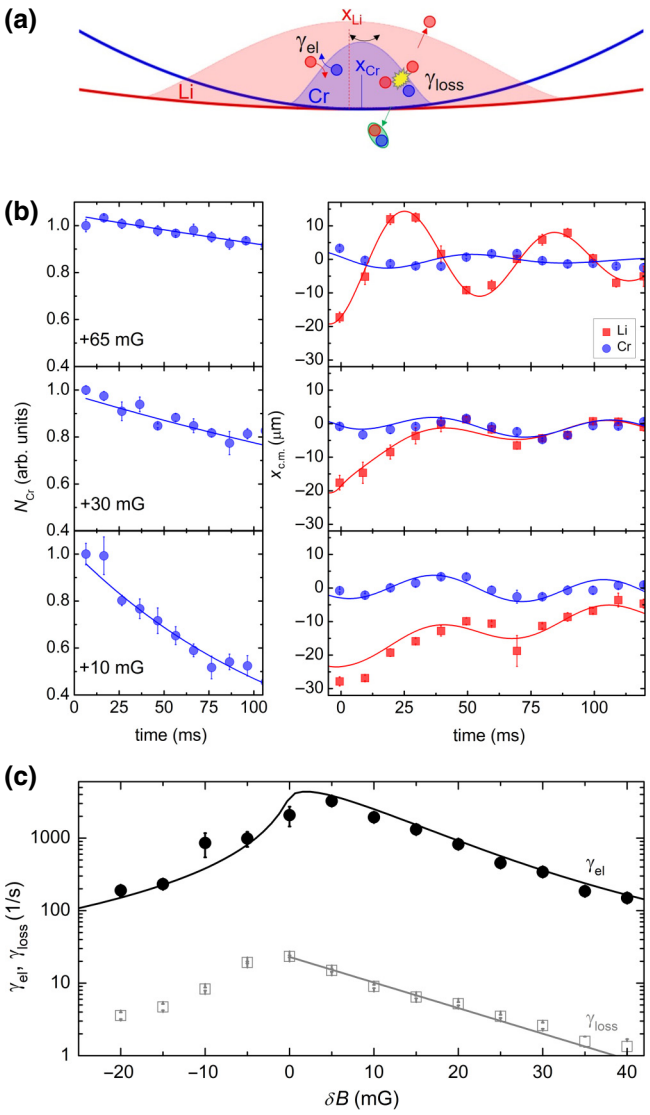

FIG. 2. Elastic and inelastic scattering properties of resonantly interacting Li-Cr Fermi mixtures. (a) Sketch of the experimental configuration employed to simultaneously extract $\gamma_{\rm loss}$ from the minority Cr number evolution, and $\gamma_{\rm el}$ from the Li and Cr c.m. dynamics through the analysis developed in Refs. [32–35]; see the text for details. (b) Examples of the observed dynamics, recorded at different magnetic field detunings specified in the legend, of the chromium atom number (left panels), and of the centers of mass of both Cr (blue circles) and Li (red squares) components (right panels). Lines are best fits to the data of the models described in the text, through which we extract $\gamma_{\rm loss}$ and $\gamma_{\rm el}$, respectively. (c) Experimentally determined rates for elastic (filled circles) and inelastic (open squares) collision events per Cr atom, as a function of the magnetic field detuning δB. Black and gray curves are best fits of $\gamma_{\rm el}$ and $\gamma_{\rm loss}$, respectively, to the theoretically expected trends; see the text for details.

We simultaneously measure these two observables as a function of the magnetic field detuning $\delta B = B - B_0$, where B_0 is the FR pole, through the study of in-trap collective-mode dynamics; see the sketch in Fig. 2(a). Our probing method is based on the simultaneous monitoring, as a function of time, of the atom numbers $N_{\rm Cr}$ and $N_{\rm Li}$, as well as of the axial sloshing of both species in terms of their center-of-mass (c.m.) coordinates. Fitting exponential decays to the minority Cr atom number yields $\gamma_{\rm loss}$ associated with the dominant three-body Li-Li-Cr recombination process; see Appendix D. The elastic collision rate $\gamma_{\rm el}$ is instead extracted from the analysis of the c.m. evolution of the two mixture components via a two-coupled harmonic oscillator model [32–35]; see Fig. 2(b) and Appendix C for details of the model. Fitting the c.m. position of the atomic clouds $x_{\rm c.m.}$ as a function of time and taking into account the observed atom number loss, $\gamma_{\rm el}$ can be extracted reliably.

The measurement starts by preparing a noninteracting Li-Cr mixture within the sole IR trapping beam near the zero crossing of the selected FR, at an initial detuning $\delta B \sim +0.48$ G. After selectively displacing the Li cloud slightly out of the axial potential minimum at $x = 0$, while leaving Cr unaffected, we quickly set δB to variable values around the FR pole; see Fig. 2(a). We then monitor the subsequent number and c.m. evolution as a function of time. At the initial detuning, i.e., under noninteracting conditions, the atom losses are negligible, lithium undergoes small, undamped oscillations with single oscillation frequency of about 17 Hz. Simultaneously, chromium, which features a bare trapping frequency of 14 Hz, is found at rest at all evolution times. As the resonance is approached, effects of both inelastic and elastic processes become more pronounced. Examples of the observed dynamics at various $\delta B > 0$ are presented in Fig. 2(b) in order of increasing interaction strength from top to bottom. Here we show the minority chromium number $N_{\rm Cr}$ (left panels) and c.m. coordinates for both species (right panels) as a function of time. The Cr number evolution, always well fitted by a single exponential decay [see the solid lines in the left panels of Fig. 2(b)], reveals a progressively reduced lifetime (increased loss rate), as the resonance pole is approached from above, $\delta B \to 0^+$. Parallel to this, the centers of mass of the two mixture components exhibit more interesting dynamics, which qualitatively change close enough to the FR pole. In particular, for $\delta B \gtrsim 30$ mG (small interaction strength), we observe a damping of the Li c.m. oscillations—accompanied by weak damped oscillations of the Cr cloud at its bare axial frequency. This damping becomes progressively more pronounced as δB is reduced, consistently with the expected behavior in the collisionless regime [32–35]. For $\delta B \lesssim 30$ mG, instead, the barycenters of the two clouds exhibit weakly damped, in-phase oscillations, characterized by one single frequency, intermediate between the unperturbed Li and Cr ones. This observation is consistent with a collisionally hydrodynamic behavior of our Fermi mixture near the FR center, expected to arise in the strongly interacting region, once $\gamma_{\rm el}$ greatly exceeds the axial trap frequencies [32–35]; see Appendix C for more

details. Despite the c.m. evolution drastically changing between the collisionless and the hydrodynamic regimes, it is well reproduced at all detunings by the coupled oscillator model, with γ_{el} as the only free parameter; see the best-fit curves in the right panels of Fig. 2(b).

The main results of this characterization are summarized in Fig. 2(c), which shows the experimentally determined γ_{el} (filled circles) and γ_{loss} (open squares) as a function of the magnetic field detuning across the resonance region. The inelastic loss rate, for $\delta B \geq 0$, exhibits an exponential growth [gray line in Fig. 2(c)] as the resonance pole is approached, in qualitative agreement with the trend expected for the three-body recombination rate coefficient near a narrow FR [36]; see Appendix D for more details. After reaching a maximum value at $\delta B \sim 0$, the extracted γ_{loss} is found to progressively drop as the field is further decreased, consistent with previous observations on other atomic systems [36]. However, since in this $\delta B < 0$ region Feshbach dimers can be formed and contribute to the detected atom signal, γ_{loss} can no longer be interpreted solely in terms of three-atom recombination processes, and its theoretical analysis goes beyond the scope of the present study.

Contrarily to the inelastic case, γ_{el} can be analyzed as an elastic Li-Cr scattering rate across the entire region of explored detunings. We obtain the theory estimate as $\gamma_{el} = \langle n_{Li}\rangle_{Cr}\langle\sigma(B)v\rangle_T$ [37], with $\sigma(B)$ denoting the magnetic-field-dependent cross section for Li-Cr collisions, v the relative velocity, $\langle n_{Li}\rangle_{Cr}$ the Li density averaged over the Cr cloud, and $\langle\cdot\rangle_T$ thermal averaging; see Appendix C for details. Since the overlap density and temperature of the sample are directly accessible via absorption imaging, and since $\sigma(B)$ is completely determined by the parameters of our FR [29] (see Appendix C), we are left with the FR pole location B_0 as the only free parameter. The theory fits the experimental γ_{el} remarkably well across the entire FR region; see the solid black line in Fig. 2(c). This allows us to pinpoint the resonance pole with ±3-mG accuracy.

Finally and most importantly, the Fig. 2(c) data reveal the collisional stability of the Li-Cr mixture under resonant interactions. This is signaled by the elastic rate greatly exceeding the inelastic one over a comparably wide range of magnetic field detunings across the Feshbach resonance, with a *good-to-bad* collision ratio $\gamma_{el}/\gamma_{loss}$ found to reach values up to 200. We ascribe the observed stability to the fact that, in spite of the narrow nature of the FR used [29], three-body processes involving identical fermions are suppressed by antibunching due to Fermi statistics of our mixture components [30,38], relative to the bosonic case. As shown in the following section, this is extremely advantageous for the efficient magnetoassociation of LiCr dimers and, more generally, it is very promising in light of future many-body studies of strongly interacting Li-Cr Fermi mixtures.

Despite the data on elastic and inelastic properties of our system presented here being taken on Li$|1\rangle$-Cr$|1\rangle$ mixtures across the most promising *s*-wave FR, a similar characterization has also been conducted on Li$|2\rangle$-Cr$|1\rangle$, yielding essentially identical results.

III. PRODUCTION OF HIGH PHASE-SPACE DENSITY LiCr SAMPLES

We now move to investigate the conversion process into LiCr Feshbach molecules via magnetoassociation. We first characterize the molecule conversion efficiency as a function of the magnetic B-field sweep rate across the FR, and then explore how the number of LiCr dimers depends on the initial atomic samples to maximize the final molecule PSD. In order to experimentally show LiCr dimer formation, count their number, and characterize their density or momentum distribution, here and in the following sections we use negative or positive signals depending on the task at hand; see Appendices D and E. By negative signals we denote atomic loss signals that unambiguously determine the molecule number. This is relatively straightforward in our system, where two-body losses are absent and three-body recombination is much slower than typical molecule association times, so that only atoms bound into molecules are lost. Positive signals instead only originate from previously associated atoms, which give rise to a measurable optical density on the atomic Li and Cr imaging transitions; see Sec. IV B below. In our experiment we employ two different schemes to obtain positive signals. The first one relies on Stern-Gerlach separation, where the molecule cloud is spatially resolved from the atomic ones thanks to a different acceleration and a sufficiently long time of flight (TOF). The second method exploits fast (few hundred microsecond-long) rf transfers of unpaired Li and Cr atoms to dark states that do not interact with the imaging light. Only positive signals allow access to further information about the molecule sample, such as thermodynamic quantities.

A. Two-body adiabaticity

Magnetoassociation is the adiabatic conversion of scattering atom pairs into weakly bound molecules, induced by a magnetic field sweep across the FR pole from the attractive ($B_i > B_0$) to the repulsive side ($B_f < B_0$); see Fig. 3(a). The efficiency of this process depends on the Feshbach resonance parameters, the conditions of the parent atomic gases, and the magnetic field sweep rate [39]. We exploit a positive molecule signal obtained from direct absorption imaging to reveal the sensitivity of the associated molecules to the final magnetic field detuning; see Fig. 3(b). We typically observe a sharp rise from zero background to saturation in a B-field region of a few tens of milligauss. Alternatively, leveraging on the stability of our Fermi mixtures, a negative signal can be used to quantify

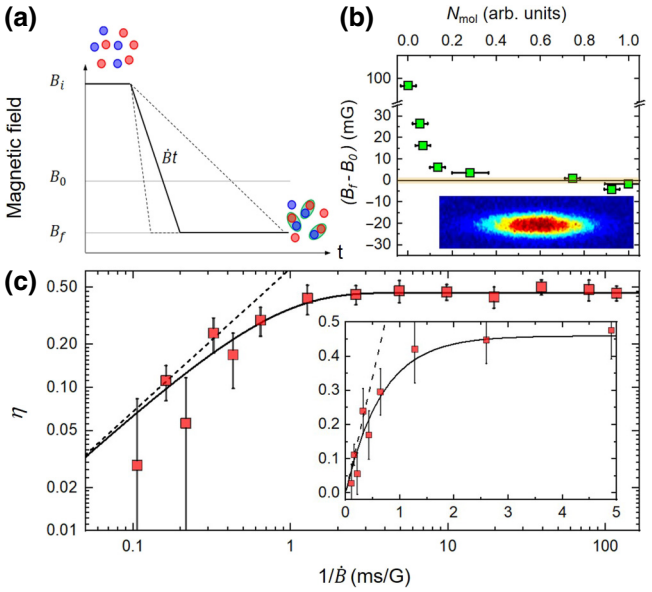

FIG. 3. Magnetoassociation efficiency and two-body adiabaticity. (a) Sketch of the experimental sequence: the magnetic field is swept from B_i across the FR pole B_0 down to $B_f < B_0$ with variable rate $\dot{B}$, after which the number of created molecules is measured through either positive or negative signals; see the text for details. (b) Normalized number of molecules formed via magnetoassociation as a function of B_f across the FR for fixed $\dot{B} = 90$ ms/G. The inset is an example of a positive signal of LiCr via direct absorption imaging with Li light after a 2-ms TOF. (c) Association efficiency η referenced to the Cr minority component as a function of the inverse ramp speed $1/\dot{B}$. The solid black line shows the best functional fit of Eq. (1) to the data and the dashed line its approximation in the fast-sweep limit.

the number of associated molecules. Indeed, after a short hold time following the B-field sweep, only atoms that were converted into dimers are (entirely) lost, and the conversion efficiency is nothing but the fractional loss between the initial and final atom numbers; see Appendix D. We measure the association efficiency as the fractional loss of the Cr minority component as a function of the inverse magnetic sweep rate $1/\dot{B}$; see Fig. 3(c). We start the experiment by preparing the Li$|1\rangle$-Cr$|1\rangle$ mixture about +100 mG above the resonance. Li$|1\rangle$ is degenerate with $T/T_F = 0.20(5)$ at $T = 170$ nK and a peak density of $1.3(2) \times 10^{12}$ cm^{-3}, while Cr$|1\rangle$ is essentially thermal $T/T_F \simeq 1$ at $T = 240$ nK with a peak density of $0.74(3) \times 10^{12}$ cm^{-3}. The magnetic field is swept to $\delta B < 0$ with variable ramp speed, after which we measure the number of associated molecules.

As for other experiments, our results are well captured by a Landau-Zener model [40–45]. According to Ref. [45], we fit the following functional form to the data:

$$\eta = \eta_0 \left[1 - \exp\left(- \frac{\Gamma \langle n_{\mathrm{Li}} \rangle_{\mathrm{Cr}}}{\eta_0} \frac{1}{\dot{B}} \right) \right]. \tag{1}$$

Here η_0 represents the saturated efficiency, $\langle n_{\mathrm{Li}} \rangle_{\mathrm{Cr}}$ is the density of the majority component averaged over the density of the minority one, and Γ is only a function of the collision parameters, i.e.,

$$\Gamma = \frac{(2\pi)^2 \hbar}{m} a_{\mathrm{bg}} \Delta B, \tag{2}$$

where $a_{\mathrm{bg}} = 41.48(3)\, a_0$ is the background s-wave scattering length, $\Delta B = 0.48$ G is the magnetic field width, and m is the reduced mass. While the adiabatic regime ($\eta \simeq \eta_0$) depends on the overall PSD overlap of the atomic mixture and lacks an analytical description to date, the fast-sweep regime, where $\eta \simeq \Gamma \langle n_{\mathrm{Li}} \rangle_{\mathrm{Cr}} / \dot{B}$, can be straightforwardly tested against the experimental results. From a functional fit of Eq. (1) with an observed Li$|1\rangle$ density averaged over the Cr$|1\rangle$ cloud of $\langle n_{\mathrm{Li}} \rangle_{\mathrm{Cr}} = 0.62(5) \times 10^{12}$ cm^{-3}, we derive $\Gamma_{\mathrm{exp}} = 1.1(1) \times 10^{-12}$ cm^3 G/ms; see the solid line in Fig. 3(c). The dashed line marks the linear, fast-sweep regime. The fitted Γ_{exp} is in satisfactory agreement with the theory prediction of $\Gamma_{\mathrm{th}} = 0.479 \times 10^{-12}$ cm^3 G/ms. The mismatch of about a factor of 2 might be due to an underestimation of the overlap density during molecule association, where the mixture experiences strong attractive interactions. We stress that, as expected from the extremely favorable mixture stability shown in Sec. II, we can perform magnetoassociation with field rates slower than the two-body adiabatic criterion by more than 2 orders of magnitude without affecting efficiency and the molecule number.

B. Optimization and molecule PSD

In order to identify the best working conditions, we characterize the molecule association efficiency as a function of the Li-Cr density overlap, deep in the two-body adiabatic regime ($1/\dot{B} = 90$ ms/G). This is accomplished by only varying the number of atoms initially loaded into the BODT with fixed evaporation and final trap parameters. In this experiment we spatially resolve atomic and molecular clouds thanks to Stern-Gerlach separation and simultaneously count the number of Li, Cr, and LiCr. Figure 4(a) shows the associated molecule number as a function of the pair density $\langle n_{\mathrm{Li}} n_{\mathrm{Cr}} \rangle = \int n_{\mathrm{Li}} n_{\mathrm{Cr}} d\mathbf{r}$. On general grounds, neglecting atom-molecule thermalization, the molecule number depends on the PSD overlap between the parent atomic clouds during association [45,46]. However, for Maxwell-Boltzmann gases at constant temperature, this is proportional to $\langle n_{\mathrm{Li}} n_{\mathrm{Cr}} \rangle$. Since, for this experiment, $T_{\mathrm{Cr,Li}}$ are kept constant, with $T_{\mathrm{Cr}}/T_{F,\mathrm{Cr}} \geq 0.5$ and almost constant $T_{\mathrm{Li}}/T_{F,\mathrm{Li}} = 0.30(5)$, we expect this relation to hold to first approximation. Indeed, the experimental data are well captured by a linear fit, as shown by the solid black line in Fig. 4(a).

From the same experimental data we also extract the conversion efficiency η as a function of $\langle n_{\mathrm{Li}} \rangle_{\mathrm{Cr}}$; see

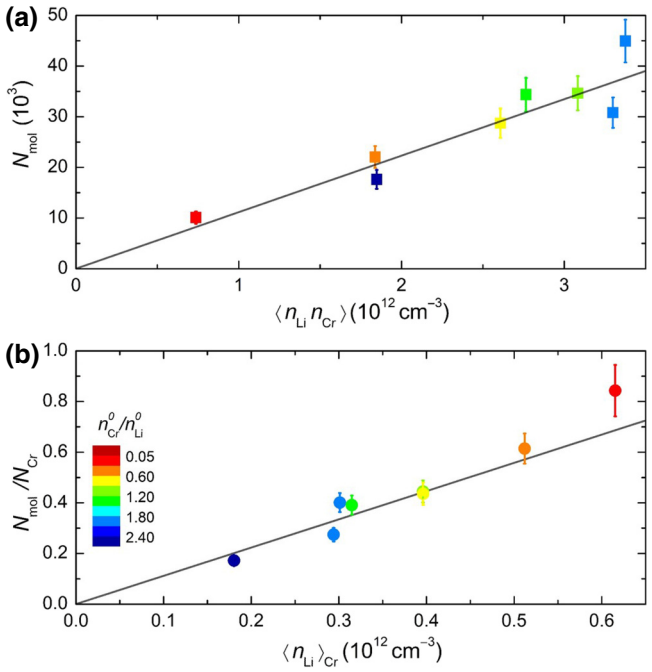

FIG. 4. (a) Number of associated molecules N_{mol} as a function of the Li-Cr pair density $\langle n_{Li} n_{Cr} \rangle$. The black line shows a linear fit to the data with zero intercept. (b) Magnetoassociation efficiency with respect to Cr as a function of the Li density averaged over the Cr cloud $\langle n_{Li} \rangle_{Cr}$. The black line shows a linear fit to the data with zero intercept. In both panels the same color code indicates the corresponding imbalance between the peak densities of Cr and Li atomic clouds.

Fig. 4(b). We stress that, although Cr atoms are always lower in number compared to Li atoms, except for the leftmost point of Fig. 4(b) with lowest Li density, their peak density can overcome the Li one. Hence, through this characterization, we explore different regimes in which the majority component is locally either Cr or Li; see the color map. Also in this case, η exhibits a linear increase with $\langle n_{Li} \rangle_{Cr}$, showing no saturation effects up to the highest densities explored herein. Comparing Figs. 4(a) and 4(b), we see that intermediate mixture imbalance enables the production of the largest molecule samples, of nearly 5×10^4 molecules, and a comparatively good conversion efficiency of 40% to 50%. These results are in line with the value reported on ^{6}Li ^{40}K Feshbach molecules [44,47] and higher than the 30% efficiency shown on ^{40}K ^{161}Dy [24]. However, our data also show a maximum conversion efficiency of about 80%, at the expense of a lower but still considerable molecule number of $2 \div 3 \times 10^4$. This regime is comparable with results on deeply degenerate homonuclear spin mixtures of ^{40}K [42], where both components shared the same degree of degeneracy. The ability to create large molecule samples with tunable density imbalance of the parent mixture may help in the future to sympathetically cool molecules down to degeneracy with leftover Cr atoms, which do not limit the molecule lifetime at our typical densities; see Sec. V below.

As shown in Fig. 4 the molecule population sensitively depends upon the Li-Cr pair density of the initial atomic mixture. After careful optimization, we study the ballistic expansion of Feshbach dimers after variable time of flight via the Stern-Gerlach separation method, and compare it with the expansion of the atomic clouds. After the BODT is switched off, atoms and molecules expand into the magnetic saddle potential generated by our coils. We obtain our record PSD starting magnetoassociation with atom numbers $N_{Li} = 3 \times 10^5$ and $N_{Cr} = 1 \times 10^5$ and temperatures $T_{Li} = 0.15 T_F = 70$ nK and $T_{Cr} = 0.5 T_F = 180$ nK. From this starting condition we obtain $36(4) \times 10^3$ molecules at 180 nK, with peak spatial density of $0.75(10) \times 10^{12}$ cm^{-3}, and peak PSD of $n_{LiCr} \lambda_{dB}^3 = 0.12(2)$, where $\lambda_{dB} = \sqrt{2\pi\hbar^2/(m k_B T)}$ is the corresponding de Broglie wavelength. Our result compares well with the highest reported PSDs in other mass-imbalanced Fermi mixture experiments [24,31], and even higher LiCr PSDs may be obtained by adding a crossed BODT [28], not employed in the present work. Although the magnetoassociation ramp is deep in the adiabatic regime for the two-body problem, the molecular sample has not reached full thermal equilibrium. This last point, together with the possibility to further evaporate Cr, thereby sympathetically cooling LiCr, will be the subject of a future study.

IV. PROPERTIES OF FESHBACH DIMERS

In this section we directly measure the magnetic dipole moment μ_b of the newly created LiCr Feshbach molecules and reveal its dependence upon the magnetic field detuning δB from the FR pole, following a strategy similar to Ref. [24]. Furthermore, we devise a new all-optical method that allows for an independent measurement of the so-called open-channel fraction of the Feshbach state and of its binding energy.

A. Magnetic dipole moment

We first accurately measure μ_b at fixed $\delta B = -4$ mG to reveal a deviation with respect to the atomic values of Li and Cr, which at this bias field are respectively $\mu_{Li} = 1\mu_B$ and $\mu_{Cr} = 6\mu_B$ within a few per mille. To this end, we perform a Stern-Gerlach-type experiment and record the temporal evolution of the vertical center-of-mass positions $z_{c.m.}$ of Li, Cr, and LiCr under the application of a vertical magnetic field gradient $\partial_z B$. We prepare the LiCr sample under the optimal conditions found in Sec. III and switch off the BODT immediately after molecule creation, letting the particles expand under the combination of the gravitational and the species-dependent magnetic forces. For each component, the c.m. acceleration is $g + \mu_X \partial_z B / m_X$, where g is the gravitational acceleration, μ_X is the magnetic dipole moment of species X, and m_X is

the corresponding mass. The magnetic field gradient $\partial_z B$ is calibrated on the observed $z_{\mathrm{c.m.}}^{\mathrm{Li,Cr}}$, and μ_b is obtained from a single-parameter fit to the LiCr trajectory; see the data and fit in Fig. 5(a). The extracted value $\mu_b = 5.85(5)\mu_B$, clearly resolved from both the atomic counterparts, markedly differs from the magnetic moment of the (closed-channel) molecule state inducing the FR $\mu_{\mathrm{CC}} = 5\mu_B$, pointing to a sizable admixture with the open-channel wave function, with $\mu_{\mathrm{OC}} = 7\mu_B$.

In order to better understand our observations, it is instructive to express the Feshbach dimer wave function as a superposition of open- and closed-channel components [18,37,39]:

$$|\psi_b(R)\rangle = \sqrt{1-Z}\phi_{\mathrm{OC}}(R)|\mathrm{OC}\rangle + \sqrt{Z}\phi_{\mathrm{CC}}(R)|\mathrm{CC}\rangle \quad (3)$$

with the unit-normalized radial wave functions $\{\phi_{\mathrm{OC}}(R), \phi_{\mathrm{CC}}(R)\}$ referring to the open- and closed-channel components with spin states $\{|\mathrm{OC}\rangle, |\mathrm{CC}\rangle\}$, respectively. The closed-channel fraction Z, bound to be $0 \leq Z \leq 1$, determines the character of the Feshbach molecule: from open-channel like for $Z \to 0$ to closed-channel like for $Z \to 1$. The Feshbach dimer has energy E_b and magnetic moment $\mu_b = \partial_B E_b$. These, if referenced to the scattering continuum, define the binding energy $\epsilon_b = E_{\mathrm{OC}} - E_b$ and the differential magnetic moment $\delta\mu_b = \mu_{\mathrm{OC}} - \mu_b$, which are linked to Z via the Hellmann-Feynman theorem [18,48]:

$$\mu_b = Z\mu_{\mathrm{CC}} + (1-Z)\mu_{\mathrm{OC}}. \quad (4)$$

An analytical solution for $Z(\delta B)$ is available in the effective range expansion [49]

$$Z = 1 - \frac{1}{\sqrt{1 + 4R^*/(a - a_{\mathrm{bg}})}} \quad (5)$$

with $a(B)$ the scattering length, a_{bg} its background value, and $R^* = \hbar^2/(2ma_{\mathrm{bg}}\Delta B\delta\mu)$ the effective range parameter. Equations (4) and (5) thus provide the expected magnetic field dependence of μ_b, ranging for LiCr from $\mu_{\mathrm{CC}} = 5\mu_B$ for $Z \to 1$ to $\mu_{\mathrm{OC}} = 7\mu_B$ for $Z \to 0$.

We reveal and experimentally characterize the field dependence of μ_b, thereby confirming the paramagnetic nature of LiCr closed-channel molecules. In this case we let the particles expand for a fixed TOF after the BODT is switched off and record the $z_{\mathrm{c.m.}}$ of the LiCr cloud as a function of δB. In order to minimize temporal and spatial variation of the magnetic field experienced by the molecules, we employ a short TOF of 3.5 ms with a 200-μs-long rf cleaning pulse on Cr right before the imaging pulse. Knowledge of the initial *in situ* position of the atoms and the B-field landscape allows us to directly extract $\mu_b(\delta B)$, which is shown in Fig. 5(b).

A fit of Eq. (4) to the data, with $Z(B)$ given by Eq. (5) and B_0 as the single fitting parameter, yields the solid black line in Fig. 5(b). We find good agreement with the experimental results, and ascribe the residual discrepancy to the B-field inhomogeneity experienced by the molecules during the TOF. We stress that these results show our high degree of control over the applied magnetic field and, most importantly, the paramagnetic nature of the LiCr closed-channel molecule. Moreover, the observed trend of μ_b, asymptotically approaching $\mu_{\mathrm{CC}} = 5\mu_B$, confirms the FR assignment of our quantum collisional model for Li-Cr developed in Ref. [29] and shows our ability to controllably populate the least bound vibrational level of the $X\,^6\Sigma^+$ ground-state potential. This is extremely convenient for future STIRAP transfer to the LiCr absolute ground state, which only requires a change in the vibrational degrees of freedom and circumvents the need for an optically excited state with sizable overlap with both electronic ground-state multiplicities as in other experiments [50]; see Sec. VII below.

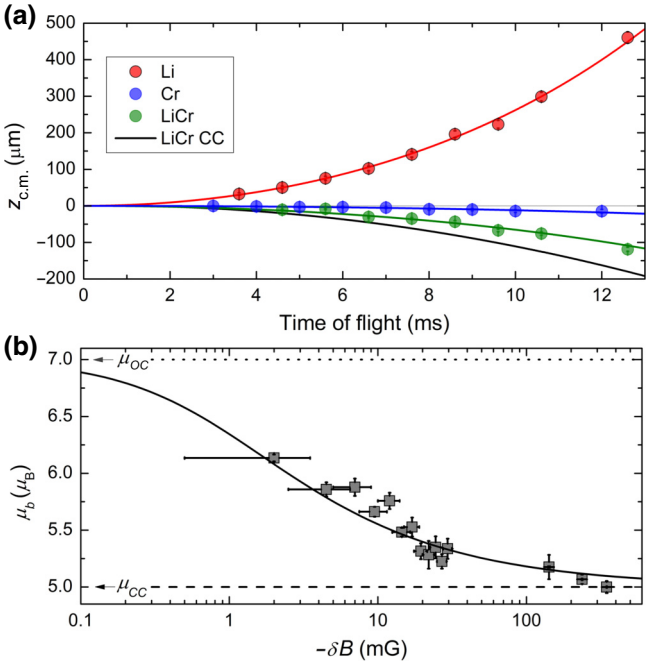

FIG. 5. (a) Vertical center-of-mass trajectories for atoms and molecules in time of flight. The red, blue, and green circles show the evolution of the c.m. in the vertical direction as a function of the TOF for Li, Cr, and LiCr, respectively. The corresponding lines with matching color code show the fitted theory curves. The black line represents the expected trajectory for a purely closed-channel molecule ($Z = 1$). (b) Magnetic dipole moment μ_b of LiCr Feshbach molecules as a function of the absolute B-field detuning from the FR pole. The black curve represents the theory prediction based on Eqs. (4) and (5) with only the resonance position B_0 as the fitting parameter. The dotted and dashed lines respectively mark the magnetic moments of the scattering atom pair μ_{OC} ($Z = 0$) and of the closed-channel molecule μ_{CC} ($Z = 1$).

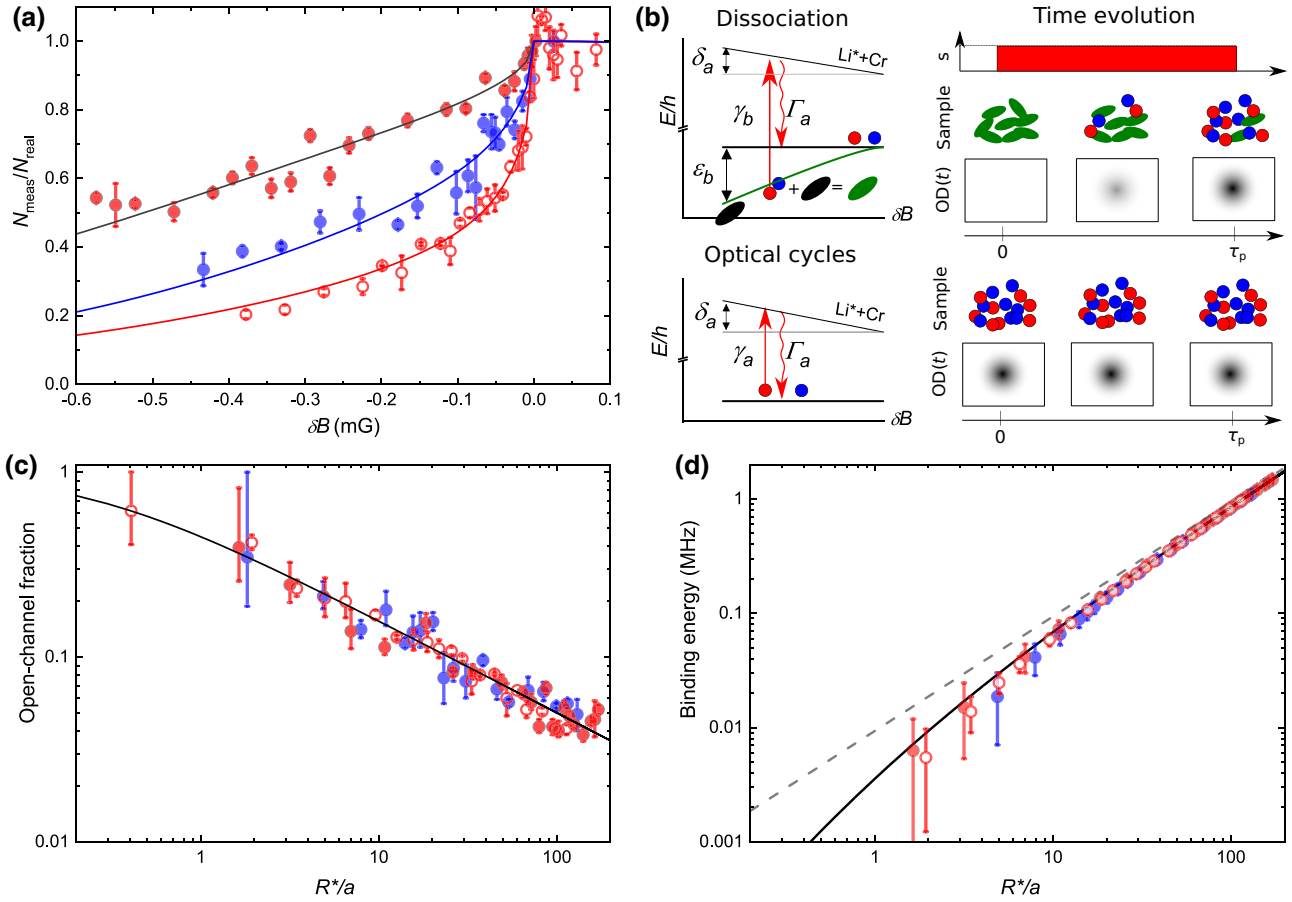

FIG. 6. Optically determined open-channel fraction as a function of detuning from the resonance. (a) Counted molecule number N_{meas}, normalized to the real one N_{real}, derived from *in situ* absorption pictures taken on the Li (red circles) and Cr (blue circles) imaging transitions on pure molecular samples. We show a comparison between a longer (filled circles) and shorter (open circles) pulse time with the same laser intensity within 10%. The red filled circles are taken with $\tau_P = 40$ μs and $I_0 = 0.24$ mW cm^{-2}, the red open circles with $\tau_P = 11$ μs and $I_0 = 0.2$ mW cm^{-2}, and the blue circles with $\tau_P = 21$ μs and $I_0 = 0.76$ mW cm^{-2}. The solid lines show our model prediction equation (8) with only a common field offset as the fitting parameter and Z given by Eq. (5). (b) Sketch illustrating the model explained in the main text. The top-left panel shows the dissociation mechanism at rate γ_b induced by the imaging laser resonant at $\delta B = 0$ with the lithium atomic transition of natural width Γ_a: a detuning of $\delta_m = \delta_a + \epsilon_b$ is acquired for finite $\delta B < 0$. The bottom-left panel shows the optical cycles Li atoms undergo after molecule dissociation at rate γ_a. The right panels show (from top to bottom) the pulse shape of duration τ_p, the time-dependent OD of the initial molecule sample, and, as a comparison, the constant OD of an atomic sample. (c),(d) The open-channel fraction and binding energy as a function of R^*/a, extracted with our model equation (8) from the three datasets in panel (a) (with the same symbol choice), together with the theory predictions given by Eqs. (5) and (9), respectively (solid black lines); see Appendix E for details.

B. Optical measurement of open-channel fraction and binding energy

As anticipated in the previous section discussing our magnetic moment measurement (see Fig. 5), the closed-channel fraction represents an essential feature of the Feshbach dimer. Besides μ_b, Z also determines the collisional stability of Feshbach molecules, as well as the outcome of future STIRAP transfer schemes to deeply bound states. While the former is longest for $Z \to 0$, the latter is optimal for $Z \to 1$. An accurate measurement of $Z(\delta B)$ close to a narrow FR at high B field is technically challenging. Indeed, wiggle spectroscopy [51] has limited temporal resolution, rf spectroscopy [41,52] requires high rf power, potentially perturbing the B-field stabilization, photoassociation techniques [53] require an optically excited molecule level and laser light to address it, and, finally, magnetic moment spectroscopy [see the previous section and Ref. [24]] suffers from field inhomogeneity and temporal constraints. Here we overcome these issues by developing a convenient and rather general optical method, which exploits absorption imaging of Feshbach dimers with laser light addressing transitions of the parent atomic species. Our method is based on the analysis of the systematic reduction of the molecule signal, recorded as a function of δB, a rather generic trend already reported for various systems; see, e.g., Ref. [45]. Such a

seeming drop of the dimer population is illustrated for LiCr in Fig. 6(a), which shows the measured number N_{meas} normalized to the real one N_{real} as a function of δB, both for Li (red circles) and Cr (blue circles) imaging lights. For Li, we further compare a long (filled circles) with a short (open circles) pulse duration. One can note how, despite quantitative differences, in all cases $N_{\mathrm{meas}}/N_{\mathrm{real}}$ monotonically decreases with increasing $|\delta B|$. While this effect was previously interpreted in terms of an effective imaging cross section, in the present case the particle number sensitivity on the imaging parameters confutes such an interpretation, and we here propose a different one. Our main idea, sketched in Fig. 6(b), is that the absorption signal of dimers results from the optical density of the atoms, into which molecules are dissociated during the imaging pulse at a rate γ_b given by the bare atomic scattering rate γ_a weighted by the dimer open-channel fraction $1-Z$. Building on such an intuition, we develop our model, described below in more detail, that allows us to establish a univocal link between $N_{\mathrm{meas}}/N_{\mathrm{real}}$ on one side, and $1-Z$ and the binding energy (ϵ_b) on the other. Hence, this simple theory can be employed to either predict $N_{\mathrm{meas}}/N_{\mathrm{real}}$ once Z and ϵ_b are known [see the lines in Fig. 6(a) based on Eq. (5)], or vice versa to obtain those quantities from the experimentally recorded dimer signal [see Figs. 6(c) and 6(d)]] without relying on any *a priori* knowledge. In the following, we review our model and results in more detail.

Our model holds under three main assumptions [see also the sketch in Fig. 6(b)]: (i) closed-channel molecules do not directly interact with the atomic imaging light; (ii) Feshbach dimers are dissociated by the imaging light at a rate given by Fermi's golden rule $\gamma_b = \gamma_a |\langle \psi_b | \mathrm{OC} \rangle|^2 = \gamma_a(1-Z)$, with γ_a denoting the atomic scattering rate; (iii) low-intensity atomic imaging is performed on a cycling transition with atomic scattering rate $\gamma_a(s_a, \Gamma_a, \delta_a)$ dependent on the saturation parameter $s_a \ll 1$, the natural width of the transition Γ_a, and detuning δ_a. Assumptions (i) and (ii) imply that during the imaging pulse the dimer (column) density decreases as $n_{2D,b}(t) = n^0_{2D,b} e^{-\gamma_b t}$, while the free-atom one grows as

$$n_{2D,a}(t) = n^0_{2D,b}(1 - e^{-\gamma_b t}). \tag{6}$$

Since (iii) implies that the dissociation products decay back to the same open channel of the FR, and that the addressed atomic species undergoes cycling transitions until the end of the imaging pulse, from Eq. (6) we derive the instantaneous optical density (OD)

$$\mathrm{OD}(t) = \sigma_a n^0_{2D,b}(1 - e^{-\gamma_b t}), \tag{7}$$

where σ_a is the detuning-dependent, atomic absorption cross section. This is in contrast with the standard case of an atomic sample at the same (column) density that would feature a constant optical density $\mathrm{OD}_a = \sigma_a n^0_{2D,b}$ [see the sketch in Fig. 6(b)]. For $\delta B = 0$, the molecules are dissociated, the imaging light is resonant with cross section $\sigma_a = \sigma^0_a$, and the optical density is constant and equal to $\mathrm{OD}_a = \mathrm{OD}^0_a$.

By integrating Eq. (7) over the duration τ_p of the imaging pulse, it is straightforward to obtain an analytic expression for the ratio between the measured $\overline{\mathrm{OD}}(\tau_p)$ at arbitrary detuning $\delta B < 0$ and the atomic OD^0_a. While we refer the reader to Appendix E for the general derivation, we here provide a simplified expression holding for $\mathrm{OD}^0_a \ll 1$:

$$\frac{\overline{\mathrm{OD}}}{\mathrm{OD}^0_a} = \frac{1}{1 + (2\delta_a/\Gamma_a)^2}\left(1 - \frac{1 - e^{-\gamma_b \tau_p}}{\gamma_b \tau_p}\right) \tag{8}$$

with $\delta_a(\delta B) = \mu_B \delta B$ the Zeeman frequency shift of the employed atomic transition. The dissociation rate implicitly depends on the detuning of the laser as $\gamma_b = \gamma_a(s_a, \Gamma_a, \delta_b)(1-Z)$, with $\delta_b(\delta B) = \delta_a(\delta B) + \epsilon_b(\delta B)/h$. As the right-hand side of Eq. (8) is independent of OD^0_a, it coincides with the suppression of the apparent number of Feshbach molecules, $N_{\mathrm{meas}}/N_{\mathrm{real}} = \overline{\mathrm{OD}}/\mathrm{OD}^0_a$.

As anticipated, our model (8) allows us to retrieve both the open-channel fraction $1 - Z(\delta B)$ and the binding energy $\epsilon_b(\delta B)$ of the Feshbach dimers (at all δB) from their absorption images, without any *a priori* knowledge of their functional forms. Referring the reader to Appendix E for details, in Figs. 6(c) and 6(d) we show the results of our analysis, plotting the experimentally determined open-channel fraction and binding energy as a function of R^*/a. Notably, extraction of $1-Z$ and ϵ_b from the three datasets of Fig. 6(a) yields consistent results over a wide range of detunings, from the resonant regime to the background limit, despite the different pulse parameters and atomic species employed for the imaging. Both observables are found to vary over a few orders of magnitude, in excellent agreement with the theory predictions based on Eqs. (5) and (9), respectively (solid black lines). In particular, we remark how the nonzero open-channel fraction is reflected in the dimer binding energy that deviates, near the resonance pole for $R^*/a \to 0$, from that of the bare closed-channel molecule $2\mu_b \delta B$; see the dashed line in Fig. 6(d). We emphasize that this probing method works remarkably well even at very small detunings from the FR pole. Finally, note also how the data in Figs. 6(c) and 6(d) demonstrate our experimental capability to access the resonant regime with high accuracy, despite the narrow FR at our disposal, a key point for future many-body investigation of Li-Cr mixtures.

We finally remark how our model can be employed to reproduce the observed number reduction shown in Fig. 6(a). As anticipated above, in this case we assume the field dependence of $Z(\delta B)$ from Eq. (5) and the corresponding binding energy $\epsilon_b(\delta B)$ from integration of Eq. (4)

[49], $\epsilon_b(\delta B) = \hbar^2 k_*^2/2m$ with

$$k_* = \frac{\sqrt{1 + 4R^*/(a - a_{\rm bg})} - 1}{2R^*}, \tag{9}$$

where the explicit δB dependence, via $a(\delta B)$, is omitted for simplicity of notation. Since all parameters appearing in the model are known, we only allow for a precision fit of the resonance location common to all data. The best-fit results of our model are shown as solid lines in Fig. 6(a), and reproduce our experimental observation remarkably well, regardless of the imaged species and employed pulse parameters. From this viewpoint, our model can be exploited for molecule number calibration with no need for dissociation prior to the imaging pulse, which may introduce systematic heating and excitation [54,55]. In particular, we note that the saturation parameter can be conveniently derived from the reference imaging pulse after the calibration of the camera.

V. STABILITY OF ATOM-MOLECULE MIXTURES AND LONG-LIVED LiCr SAMPLES

We now move to address another key question about the experimentally realized LiCr molecules, namely, their stability against inelastic loss processes. Since magnetoassociation results in an optically trapped mixture of LiCr dimers, together with unpaired Li and Cr atoms, various inelastic mechanisms may contribute to limit the molecule lifetime. Quite generally, these can arise both from off-resonant scattering of LiCr towards electronically excited levels—accidentally induced by the trapping lights employed in the experiment—as well as from inelastic scattering in dimer-dimer and atom-dimer collisions. As the first one-body process is concerned, we find that LiCr molecules are indeed affected by both lights of our BODT. Specifically, at constant densities, we observe a linear increase of the dimer loss rate with the intensity of both BODT beams, characterized by slopes of $\Gamma_{\rm CC} = 397(14)\ {\rm Hz/(kW\,cm^{-2})}$ and $\Gamma_{\rm CC} = 5.9(2)\ {\rm Hz/(kW\,cm^{-2})}$ for the green and IR light, respectively; see Appendix F for details. Given the much smaller photoexcitation rate observed for the IR beam, relative to the green one, it is thus advantageous to turn off the latter light when LiCr dimers are created. In this way, at our typical BODT intensities, the one-body lifetime increases from about 2 ms up to a few tens of milliseconds, allowing us to characterize the stability of the molecular sample against dimer-dimer (D-D) and atom-dimer (A-D) inelastic collisions. This is fundamental both in light of future optical spectroscopy studies, and of possible implementation of evaporative and sympathetic cooling stages of Feshbach dimers towards quantum degeneracy.

As for three-atom recombination discussed in Sec. II, Fermi-Fermi mixtures are also expected [30,31,37] to benefit from Pauli suppression for D-D and A-D inelastic collisions near the FR pole—owing to the fact that these always involve at least two identical fermions (either unpaired or paired into a shallow dimer). Specifically, the loss rate coefficients β of such processes can be substantially decreased, with respect to their off-resonant background value $\beta_{\rm bg}$, as soon as dimers acquire a sizable open-channel fraction, i.e., near the resonance pole; see Sec. IV B. While this qualitative feature is generic to any Fermi-Fermi mixture, the suppression factor $\beta(R^*/a)/\beta_{\rm bg}$ sensitively depends upon the specific mass ratio between the two constituents. For atom-dimer processes in heteronuclear systems, light-light-heavy inelastic processes are predicted to dominate over the heavy-heavy-light ones in the resonant regime [31,37]. For our specific mixture, for instance, Jag *et al.* [31] foresaw already for $R^*/a \lesssim 10$ a suppression for Cr-LiCr collisions more than one order of magnitude larger than that for Li-LiCr scattering. Moreover, one also expects in the off-resonant regime that lithium-dimer collisions are dominant, given that the background value of the A-D loss rate coefficient is theoretically given by [31] $\beta^{\rm bg}_{\rm A\text{-}D} \sim 2h R_{\rm vdW}/m_{\rm A\text{-}D}$, with $R_{\rm vdW}$ the van der Waals length and $m_{\rm A\text{-}D}$ the atom-dimer reduced mass, and that $m_{\rm Cr\text{-}D}/m_{\rm Li\text{-}D} \sim 5$. Also in light of the fact that the Li density exceeds the Cr one in our typical conditions, we observe that collisional losses of LiCr dimers are indeed dominated by Li-D scattering. This is confirmed by a measured Li-to-Cr relative loss of $\Delta N_{\rm Li}/\Delta N_{\rm Cr} = 1.93(17)$, and by the fact that, when unpaired Li atoms are removed from the sample, we do not have any detectable signature of Cr-D or D-D inelastic processes.

We characterize the magnetic field dependence of $\beta_{\rm Li\text{-}D}$ varying the endpoint of the association ramp at the Li$|1\rangle$-Cr$|1\rangle$ resonance, and tracing the molecule decay as a function of time, monitored through selective imaging with the Cr light. At each detuning, the fitted exponential decay rate, corrected for the residual trap-light-induced loss contribution, yields the collisional rate. Dividing the latter by the dimer-weighted Li density $\langle n_{\rm Li}\rangle_{\rm D}$ determined experimentally, we thus extract the inelastic rate coefficient $\beta_{\rm Li\text{-}D}$. This is shown in Fig. 7 as a function of δB; see the filled red squares. One can note how $\beta_{\rm Li\text{-}D}$ monotonically decreases down from its off-resonant value as the resonance pole is approached, exhibiting a drop that becomes progressively more pronounced as $\delta B \to 0^-$. To corroborate the interpretation of our findings in terms of Pauli suppression of collisional losses [31], we repeat the same measure, but transfer the remaining unbound lithium atoms to the nonresonant spin state Li$|2\rangle$ right after the magnetoassociation ramp. In this case, where three, rather than two, distinguishable kind of fermionic atoms are involved in the collision, we observe a rate coefficient that is constant at all detunings; see the open squares in Fig. 7. This also matches the Li$|1\rangle$-D measured background value of about $7 \times 10^{-10}\ {\rm cm^3/s}$, which agrees within a factor of 2 with the theoretical estimate [31]. Notably, as shown in the

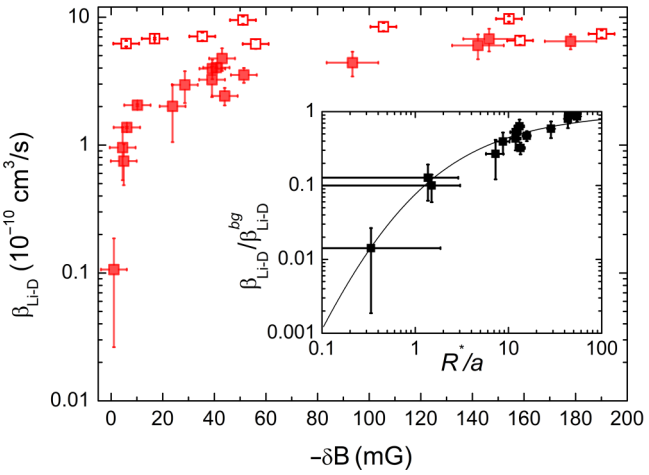

FIG. 7. Loss rate coefficient $\beta_{\text{Li-D}}$ for inelastic Li-LiCr collisions as a function of magnetic field detuning. The trend of $\beta_{\text{Li-D}}$, measured for collisions between interacting Li$|1\rangle$ and Li$|1\rangle$Cr$|1\rangle$ molecules (filled squares), is compared with the constant, nonresonant one, obtained by studying Li$|2\rangle$-dimer mixtures (open squares). The inset shows the experimentally determined $\beta_{\text{Li-D}}$, normalized to its background value $\beta^{\text{bg}}_{\text{Li-D}} = 7 \times 10^{-10}$ cm^3/s, as a function of R^*/a (black symbols), together with the theoretically predicted trend of Ref. [31]. Vertical error bars of $\beta_{\text{Li-D}}$ combine the fit, statistical and systematic uncertainties to the decay data, and the estimated mean density $\langle n_{\text{Li}}\rangle_{\text{D}}$. Horizontal error bars account for the uncertainty in the magnetic field detuning from the FR pole.

inset of Fig. 7, we find excellent agreement between the normalized experimental data $\beta_{\text{Li-D}}/\beta^{\text{bg}}_{\text{Li-D}}$ (black squares) and the predicted suppression function for Li-LiCr inelastic collisions given in Ref. [31] (solid line) as a function of R^*/a. We stress that, in spite of the narrow nature of our FR, at the smallest detunings explored here we observe up to a factor of 70^{+160}_{-35} suppression of collisional losses—a very promising value in light of future studies of resonantly interacting atom-dimer mixtures, and of the possible implementation of a final sympathetic cooling stage for LiCr molecules.

Finally, we show how the dimer lifetime can be substantially increased at *all* detunings by removing the unpaired atoms and by reducing residual trap-induced off-resonant scattering. To this end, we make use of an additional 1560-nm far-off resonant trap (FORT), whose wavelength is found to cause negligible light-induced losses (see Appendix F), consistent with zero within our experimental uncertainty. In this case we first transfer the atomic mixture from the BODT into the FORT following a 100-ms-long linear ramp, throughout which a constant trap depth for the Cr atoms is maintained. We then perform the magnetoassociation ramp, at the end of which we purify the molecule sample from the atomic components. Li atoms are removed through a spin-selective optical blast following a Li$|1\rangle \rightarrow$ Li$|2\rangle$ rf transfer. The Cr component is spilled from the FORT by further reducing the trap depth, relying on the fact that the Cr polarizability at 1560 nm is about a factor 3.5 lower than for LiCr [56,57]. While this overall procedure only reduces the initial molecule number by less than a factor of 2 at about 300 nK, it allows for a dramatic gain in lifetime even in the off-resonant regime. This is shown in Fig. 8, where the molecule number is plotted as a function of the hold time at a final, large detuning $\delta B = -100$ mG. After an initial loss—ascribable to excitation of collective modes in the LiCr cloud during the magnetoassociation and atom purification stages [see the inset of Fig. 8]—we observe a clean exponential decay of the molecule number, characterized by a time constant of 0.24(1) s. This lifetime, much longer than those measured in our system without purification nor FORT trap (limited to a few tens of milliseconds), exceeds by more than one order of magnitude that reported for LiK molecules [44] at similar peak densities, of a few 10^{11} cm^{-3}. The slow exponential decay of LiCr shown in Fig. 8 is consistent with residual evaporation dynamics within the relatively low-density molecule cloud, and it appears incompatible with intraspecies LiCr collisional losses, which will be the subject of future studies. The present measurement and analogous ones carried out without the removal of Cr atoms yield in all cases upper-bound estimates for the background values of the recombination rate coefficients, $\beta^{\text{bg}}_{\text{D-D}}$ and $\beta^{\text{bg}}_{\text{Cr-D}}$, of about 1×10^{-10} cm^3/s. This, together with the Pauli suppression of these inelastic processes [31]—expected to be even stronger than that unveiled in Li-D collisions and shown in Fig. 7—is very promising for future implementation of collisional cooling of LiCr Feshbach dimers.

VI. QUANTUM CHEMICAL MODELING

The ultracold samples of ^{6}Li^{53}Cr Feshbach dimers, thoroughly characterized in the previous sections, represent an excellent starting point for the production of a high phase-space density gas of deeply bound, paramagnetic polar molecules. Yet, LiCr is an almost unexplored species, for which spectroscopic data are completely lacking thus far, except for pioneering electron spin resonance data [25]. Its theoretical study, through advanced quantum chemical simulations, is thus crucial for two reasons: first, to gain information about the ground and electronically excited state properties of the LiCr molecule; second, to identify suitable pathways to coherently transfer LiCr Feshbach dimers to the absolute ground state [39]. In the following, we employ state-of-the-art *ab initio* quantum chemical methods to build the complete theoretical model for LiCr. By extending for the first time the portfolio of computational strategies, already applied to alkali-metal or alkaline-earth-metal dimers, to ultracold molecules containing transition-metal atoms, we obtain quantitatively accurate information on both ground and

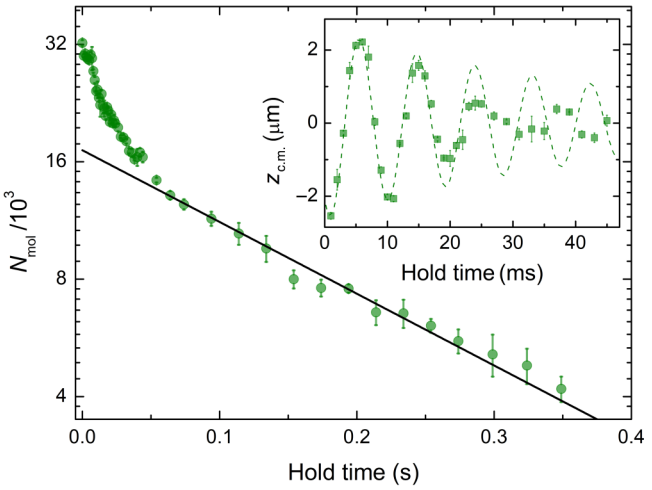

FIG. 8. Long-lived pure LiCr samples in the FORT trap at $\delta B = -100$ mG. The main panel shows the molecule number (on a log scale) as a function of the hold time, together with an exponential fit of the long-time decay yielding a time constant of 0.24(1) s. For hold times shorter than 50 ms, we observe a faster loss dynamics, which we ascribe to the initial excitation of collective modes of the LiCr sample (see the inset) induced by the magnetoassociation and purification stages.

excited electronic states, transition moments, and resulting rovibrational structure and spectra.

A. Electronic and rovibrational structure calculations

In the first step, we investigate the electronic structure of the LiCr molecule. Potential energy curves and other electronic properties are calculated within the Born-Oppenheimer approximation, including the electron correlation and relativistic effects. The two lowest electronic states, $X\,^6\Sigma^+$ and $a\,^8\Sigma^+$, dissociating into ground-state atoms, can be described very accurately using the hierarchy of the coupled cluster methods, including corrections up to the quadruple excitation level, CCSDTQ [58]. Higher-excited electronic states present a challenge, unprecedented in alkali-metal or alkaline-earth-metal molecules, because they involve high electronic spin and large orbital angular momenta of an excited Cr atom. These states are studied using the multireference configuration interaction methods, including single and double excitations and large active spaces.

We employ large correlation-consistent Gaussian basis sets with basis set cardinal numbers up to 5 [59,60] to describe all 27 electrons (three from Li and 24 from Cr). The scalar relativistic effects are included by the third-order Douglas-Kroll-Hess relativistic Hamiltonian [61,62], while the R dependence of the relativistic spin-orbit coupling is neglected. The atomic basis sets are additionally augmented by a set of bond functions to accelerate the convergence toward the complete basis set limit. The counterpoise correction is applied to reduce the basis sets' superposition errors within the supermolecule approach to interaction energy calculations [63]. All electronic structure computations are performed with the MOLPRO package of *ab initio* programs [64]. The full triple and quadruple coupled-cluster contributions are computed using the MRCC code embedded in MOLPRO [65].

In the second step, rovibrational eigenstates are calculated numerically with the exact diagonalization of the Hamiltonian for the nuclear motion within the discrete variable representation on the nonequidistant grid [66]. The atomic scattering lengths are computed using the renormalized Numerov propagator [67] with step size doubling and about 100 step points per de Broglie wavelength. Theoretical uncertainties are carefully estimated [68] by analyzing the convergence of the electronic structure calculations. More details on the employed computational and theoretical procedures, benchmarks of the used methods and basis sets, and accuracy estimations are presented in the accompanying paper [69].

B. Ground-state properties

We predict the well depths D_e of the ground $X\,^6\Sigma^+$ and first-excited $a\,^8\Sigma^+$ states to be 8769(140) and 553(11) cm^{-1} at equilibrium distances R_e of $4.87(1)a_0$ and $6.50(2)a_0$, respectively [see Fig. 1(a)]. As shown in Fig. 9, a large permanent electric dipole moment of 3.3(2) D is expected for ^{6}Li^{53}Cr in the rovibrational ground state ($v = 0$), with even slightly larger values for excited vibrational levels of $X\,^6\Sigma^+$, up to 3.4(2) D for $v = 14$. Additionally, we remark how sizable electric dipole moment values, exceeding 1 D, are already expected for comparably high vibrational states ($v \lesssim 37$) of the $X\,^6\Sigma^+$ potential; see Fig. 9. At the same time, the high-spin $a\,^8\Sigma^+$ state also exhibits a significant permanent electric dipole moment of 0.67(3) D in its $v = 0$ level (see Fig. 9), a value exceeding the largest one found for spin-triplet bialkali molecules [70].

For ^{6}Li^{53}Cr, the ground electronic state supports 46(1) vibrational levels and the dissociation energy of the $v = 0, j = 0$ level is $D_0 = 8599(140)$ cm^{-1}. The high-spin state supports exactly 16 vibrational levels with $D_0 = 512(11)$ cm^{-1}. The rotational constants B_0 for $v = 0$ levels of the $X\,^6\Sigma^+$ and $a\,^8\Sigma^+$ states are 14.02(4) and 7.67(3) GHz. The bound vibrational levels exist up to $j_{\max} = 146(2)$ for $X\,^6\Sigma^+$ and $j_{\max} = 46(1)$ for $a\,^8\Sigma^+$. Precise knowledge of the number of vibrational states allows us, via mass scaling, to infer the scattering properties of all Li-Cr isotopic combinations from accurate experimental data obtained for ^{6}Li-^{53}Cr [29,69].

C. Benchmarking the theory

The high accuracy of our *ab initio* calculation, combined with the comparably small values of both the Li-Cr

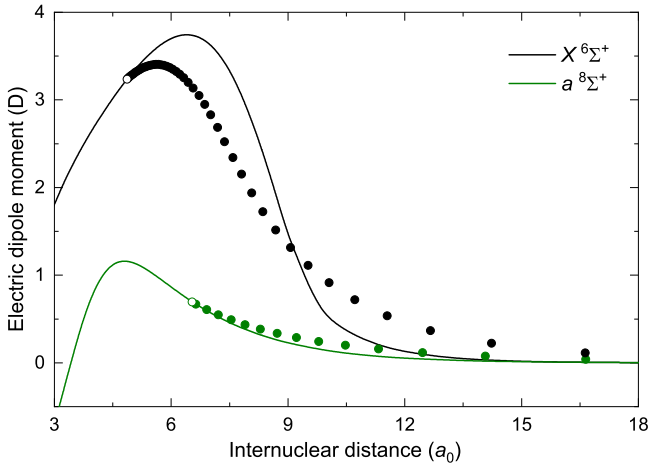

FIG. 9. Permanent electric dipole moments of the LiCr molecule in the $X\,^6\Sigma^+$ and $a\,^8\Sigma^+$ electronic states. The solid lines present them as a function of the internuclear distance. The open circles mark their values at equilibrium distances, and the filled circles present vibrationally averaged moments d_v calculated for all vibrational levels v supported by the considered electronic states placed at the corresponding vibrationally averaged internuclear distances R_v (two last points for both states are beyond the plot range).

reduced mass and well depth of the $a\,^8\Sigma^+$ state, allows us to also obtain—purely from first principles—reliable predictions for the scattering properties associated with this high-spin potential. These are encoded in the octet scattering length a_8, whose value of $41.48(2)\,a_0$ was determined with high precision in Ref. [29], as the result of a global fit of a quantum collisional model to 52 experimentally observed FRs. In this work, our *ab initio* model, without any experimental input, predicts for the ^{6}Li-^{53}Cr isotopic pair $a_8 = 49^{+48}_{-21}\,a_0$, which is in excellent agreement with the measured value. Our prediction results from a last vibrational level of the $a\,^8\Sigma^+$ state ($v = -1$) with energy $E_{-1} = -735^{+640}_{-1600}$ MHz and a van der Waals dispersion coefficient $C_6 = 954\,E_h a_0^6$ from perturbation theory [69], both in good agreement with the fitted experimental values of $E_{-1} = -1146$ MHz and $C_6 = 922(6)\,E_h a_0^6$, respectively [29]. Obtaining reliable predictions for the scattering properties of a complex, many-electron system, as the Li-Cr one, from first-principle calculations, is an extremely challenging task, and such good agreement is thus remarkable. This makes our result the first-ever scattering length prediction for atom pairs involving a transition-metal element, and Li-Cr represents the second instance, after Li-Na [68], where our *ab initio* methods could quantitatively reproduce the scattering properties between two atomic species, both heavier than H, H_2, or He.

As an additional test, our *ab initio* model correctly reproduces the order of magnitude of the subtle fine-structure corrections to the spin-spin interactions resulting from the second-order spin-orbit coupling and screening direct magnetic dipolar interactions between electrons [69]. The quantitative agreement between our *ab initio* results and our data on ultracold Li-Cr collisions [29]—governed by the least bound vibrational level and long-range tail of the interatomic potential—lets us conclude that our model can also reliably provide information, with good predictive power, on other LiCr properties, so far experimentally unexplored.

VII. OPTICAL MANIPULATION OF LiCr

As anticipated at the beginning of Sec. VI, coherent two-photon optical transfer of LiCr Feshbach dimers to the rovibrational ground state requires detailed knowledge of the intermediate, electronically excited levels of the associated transition dipole moments, and of the resulting molecular spectra—completely lacking experimental investigation so far. In the following, we employ our *ab initio* model to explore the properties of excited electronic states of LiCr, which allows us to identify suitable transitions for the efficient conversion of Feshbach dimers into tightly bound states, and more generally for the optical manipulation of LiCr.

A. Excited electronic states

Calculations of excited electronic states are significantly more challenging than those of ground ones. Excited states of the LiCr molecule are especially demanding because of the highly multireference nature of the Cr half-filled electron d shell participating in chemical bonding. In Fig. 10, we present the spectrum in Hund's case (a) representation of all molecular excited electronic states of LiCr up to the $\mathrm{Cr}(^7S) + \mathrm{Li}(^2P)$ asymptote. The states of Σ, Π, and Δ spatial symmetries with total electronic spin $S = 3/2, 5/2, 7/2$ exist. The higher-lying energy asymptote, $\mathrm{Cr}(^7P) + \mathrm{Li}(^2S)$, is above 20 000 cm^{-1}, and it will not be discussed here.

Two families of excited electronic states can be seen in Fig. 10: a first set dissociating into metastable, excited-state Cr (^5S or ^5D) and ground-state Li (^2S), and another set that dissociates into ground-state Cr (^7S) and excited-state Li (^2P). The former ones are relatively shallow, especially those associated with Cr in the ^5D state with the closed $4s^2$ shell screening interactions with the open $3d^4$ shell. The states belonging to the second family, and connected to the $\mathrm{Cr}(^7S) + \mathrm{Li}(^2P)$ asymptote, are deeper. Despite the large number of states, an avoided crossing is visible only between those with $^6\Pi$ symmetry.

The spin-orbit coupling can couple the excited electronic states of different spin and spatial symmetries. Its largest strength is expected for states dissociating into $\mathrm{Cr}(^5D) + \mathrm{Li}(^2S)$, which is asymptotically split by hundreds of cm^{-1}. Coupling of crossing states leads to avoided crossings and to enhanced mixing of different spin

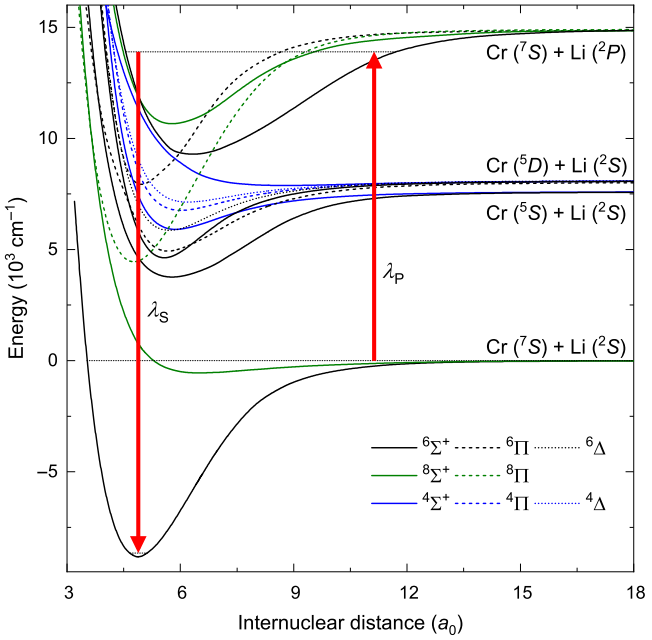

FIG. 10. Potential energy curves of the LiCr molecule in the ground and excited electronic states [in Hund's case (a) representation]. The arrows show the proposed pump and Stokes STIRAP transitions at $\lambda_P \approx 720$ nm and $\lambda_S \approx 445$ nm, respectively.

components. The spin-orbit coupling between electronic states dissociating into $\mathrm{Cr}(^7S) + \mathrm{Li}(^2P)$ should be smaller because of its negligible asymptotic value, although it might be enhanced at small internuclear distances by the presence of Cr. Although this will be discussed in more detail in the following section, we remark here how the energy landscape of LiCr, shown in Fig. 10, is significantly richer than the more familiar one of bialkali systems, and it originates from the involvement of *d*-shell electrons of Cr. While this results in a more complex scenario, the existence of metastable excited states such as $^4\Delta$—with large angular momenta and a potentially long lifetime—opens the way for applications of LiCr, primarily in the context of precision measurements [71–73], unattainable with alkali-metal dimers.

B. Prospects for STIRAP

Having provided an overview of both ground and electronically excited states of LiCr in the previous sections, we now move to discuss possible pathways for the efficient optical transfer of our Feshbach dimers towards deeply bound levels via STIRAP [74]. This method was successfully employed for a large number of alkali-metal diatomic molecules, and it involves two laser pulses that transfer coherently a molecular population between the initial and final states through an intermediate electronically excited state in a Λ configuration, while never populating it. Accurate knowledge of the energies and dipole moments of the most favorable transitions is needed to execute STIRAP successfully. While such properties can be obtained experimentally through tedious and time-consuming spectroscopic measurements, identification of suitable STIRAP pathways can be highly accelerated when guided by state-of-the-art molecular calculations presented in this work. Efficient STIRAP transfer of Feshbach dimers to the absolute ground state necessarily requires pinpointing an intermediate, electronically excited vibrational state that exhibits a significant overlap with both the initial (weakly bound, long-ranged) and the final (deeply bound, short-ranged) levels. In our search, we focus on STIRAP paths involving sextet electronic states only. Restricting our survey to this subclass is motivated by the fact that our Feshbach dimers have (almost) pure sextet character (see Sec. IV A), as that of the LiCr rovibrational ground state. This greatly simplifies our task, and the corresponding STIRAP scheme is conceptually equivalent to the singlet-to-singlet optical transfer of bialkali dimers, recently successfully employed to produce ground-state $^6\mathrm{Li}^{40}\mathrm{K}$ molecules [50].

The $(4)\,^6\Sigma^+$ and $(2)\,^6\Pi$ electronic states dissociating into $\mathrm{Cr}(^7S) + \mathrm{Li}(^2P)$ are the most promising for providing suitable intermediate levels because they are relatively well separated from other states and should be accessible at convenient optical wavelengths by strong transition dipole moments borrowed from the strong atomic transition $^2S \rightarrow {}^2P$ in Li [69]. According to our calculations, they support 54(5) and 48(4) vibrational levels, respectively, while their dissociation energies are around 5700 and 6800 cm^{-1}. Franck-Condon factors (FCFs), $|\langle v|v'\rangle|^2$, between vibrational levels supported by the ground (v) and excited (v') electronic states give the initial insight into possible optical transitions. They are presented in Fig. 11 for the relevant sextet states. The overview of the FCFs suggests the $X\,^6\Sigma^+ \rightarrow (4)\,^6\Sigma^+$ transitions [see Fig. 11(a)] as the most promising ones for the STIRAP implementation. Similar to alkali-metal dimers, the characteristic bent shape of the largest FCFs shows the existence of intermediate levels of the excited $(4)\,^6\Sigma^+$ state having noticeable overlap with both weakly and deeply bound levels of the ground $X\,^6\Sigma^+$ state. In contrast, the FCFs for the $X\,^6\Sigma^+ \rightarrow (2)\,^6\Pi$ transitions [see Fig. 11(b)] are visibly diagonal, which is not a preferable pattern for an efficient STIRAP transfer.

Figure 12 presents the FCFs for transitions from the least bound (denoted here as $v = -1$) and ground ($v = 0$) levels of the $X\,^6\Sigma^+$ ground electronic state to intermediate levels v' supported by the $(4)\,^6\Sigma^+$ excited electronic state. The largest FCFs for the "pump" transition $v = -1 \rightarrow v'$ (red symbols) are expected to connect to the most weakly bound excited-state levels just below the $\mathrm{Cr}(^7S) + \mathrm{Li}(^2P)$ atomic threshold, but values above 10^{-4} are predicted up to binding energies $E_{v'}$ of almost 3000 cm^{-1}. These FCFs also give the shape of a photoassociation spectrum. The largest FCFs for the "Stokes" transition $v' \rightarrow v = 0$ (blue

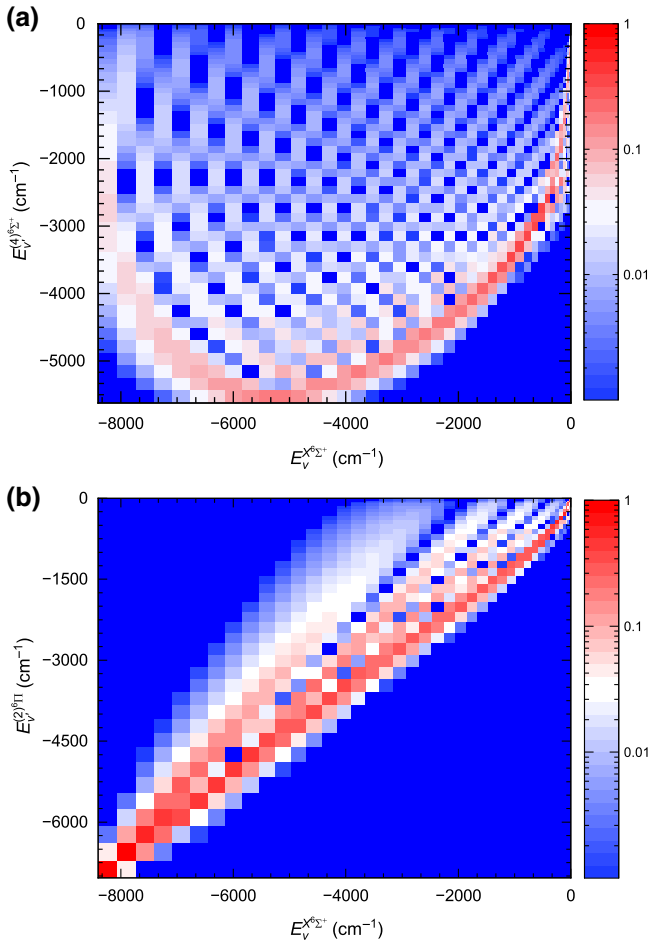

FIG. 11. Franck-Condon factors $|\langle v|v'\rangle|^2$ between vibrational levels of the LiCr molecule in the $X\,^6\Sigma^+$ ground electronic state v and $(4)\,^6\Sigma^+$ and $(2)\,^6\Pi$ excited electronic states v' as a function of their energies E_v: (a) $X\,^6\Sigma^+ \to (4)\,^6\Sigma^+$ and (b) $X\,^6\Sigma^+ \to (2)\,^6\Pi$.

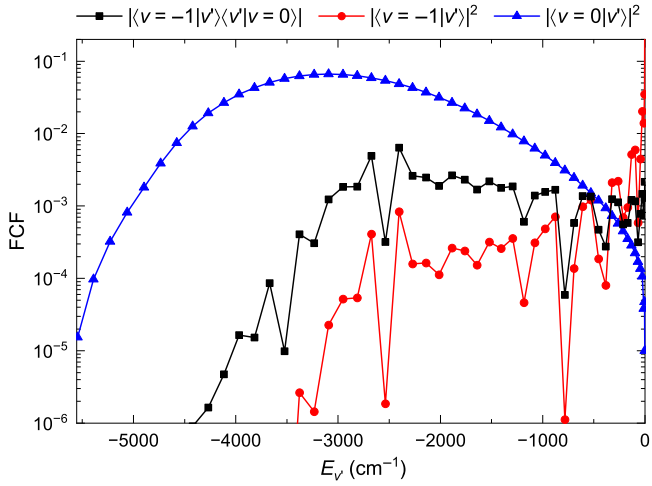

FIG. 12. Franck-Condon factors $|\langle v|v'\rangle|^2$ between the initial weakly bound $v=-1$ and final ground $v=0$ vibrational levels of the $X\,^6\Sigma^+$ ground electronic state and the intermediate vibrational levels v' with energies E'_v of the $(4)\,^6\Sigma^+$ excited electronic state and their combination $\sqrt{|\langle -1|v'\rangle|^2|\langle 0|v'\rangle|^2} = |\langle -1|v'\rangle\langle v'|0\rangle|$ for two-photon transition between the $v=-1$ and $v=0$ levels.

symbols) are found to connect to levels in the middle of the interaction potential well, with values above 10^{-2} for binding energies between 1400 and 4400 cm^{-1}. Strong Stokes transitions result from the alignment of the equilibrium distance of the $X\,^6\Sigma^+$ ground electronic state and the inner classical turning point of the $(4)\,^6\Sigma^+$ excited electronic state (see Fig. 10). The combination of the pump and Stokes FCFs govern the STIRAP. The largest two-photon FCF, $|\langle -1|v'\rangle\langle v'|0\rangle|$, of 6×10^{-3}, is found for the $v'=20$ intermediate level with a binding energy around 2400 cm^{-1}. Yet, FCFs exceeding 10^{-3} are expected for most vibrational levels with binding energies up to 3100 cm^{-1}. Thus, to avoid a large power imbalance of the pump and Stokes laser fields, intermediate v' levels with smaller binding energies around 1000 cm^{-1} can be addressed with convenient wavelengths of $\lambda_P \approx 720$ nm and $\lambda_S \approx 445$ nm, respectively; see Fig. 10.

The predicted FCFs for the $X\,^6\Sigma^+ \to (4)\,^6\Sigma^+$ transitions are similar to, or even more favorable than, those found for alkali-metal diatomic molecules, where a STIRAP transfer efficiency as large as 90% was achieved. Our predictions are robust against the uncertainty of calculated excited electronic states [69], and favorable conditions are persistent, assuming 10%–20% errors for the well depth and 0.2–0.5a_0 errors for the equilibrium distance. Including the R dependence of the transition dipole moments also does not affect the presented findings [69]. Also, spin-orbit coupling—neglected in these calculations and that could perturb some levels accidentally close to other ones of different symmetry—is expected, overall, to negligibly affect our results.

The detailed analysis of the $X\,^6\Sigma^+ \to (2)\,^6\Pi$ transitions, see Fig. 11(b), confirms that they are less suited for STIRAP, as they exhibit two-photon FCFs smaller by several orders of magnitude than those for $X\,^6\Sigma^+ \to (4)\,^6\Sigma^+$ transitions [69]. The pump FCFs are smaller because the $(2)\,^6\Pi$ potential is shallower than the $(4)\,^6\Sigma^+$ one at intermediate and large distances (see Fig. 10). The FCFs noticeably exhibit a diagonal structure that results from the accidental alignment of the equilibrium distances of the $X\,^6\Sigma^+$ and $(2)\,^6\Pi$ states. This peculiar feature, inconvenient for STIRAP, may instead allow for direct imaging, and possibly even laser cooling, of ground-state LiCr molecules. While the exact values of diagonal FCFs are very sensitive to the accuracy of underlying electronic states, our model yields FCFs robustly above 0.5 [69], sufficiently large to enable direct optical imaging of ground-state LiCr, e.g., in optical tweezers. Additionally, for our current PECs, the FCFs for $v'=0 \to v=0$, $v'=0 \to v=1$, and $v'=0 \to v=2$ transitions are predicted to be 0.94, 0.056, and

0.0007, respectively. Such a set of values is comparable to those of CaF and similar molecules, and, if experimentally confirmed, could even allow for direct laser cooling of LiCr.

VIII. CONCLUSIONS AND OUTLOOK

In summary, we have produced ultracold gases of up to 50×10^3 bosonic ^{6}Li^{53}Cr Feshbach molecules from atomic Fermi mixtures, reaching phase-space densities of 0.1 at about 200 nK. Thanks to the immunity to two-body decay and the good stability against three-body recombination of our mixture, we could perform magnetoassociation with B-field rates slower than the two-body adiabatic regime by orders of magnitude. We have directly revealed the paramagnetic nature of the LiCr electronic ground state, and demonstrated precise control of the Feshbach state via a novel optical measurement of the open-channel fraction and binding energy. Through the characterization of the relevant loss mechanisms affecting Feshbach dimers, we have identified an experimental configuration where their lifetime exceeds 0.2 s. By developing a quantum chemical model for LiCr via state-of-the-art *ab initio* methods, we have determined the fundamental properties of this new molecular species. In particular, for the rovibrational $X\,^6\Sigma^+$ ground state, we predict a large electric dipole moment of 3.3(2) D, on top of a sizable magnetic one ($5\mu_B$). Additionally, our model foresees that Feshbach dimers, already created in the least bound $X\,^6\Sigma^+$ vibrational level, can be efficiently transferred, via STIRAP through a (4) $^6\Sigma^+$ level, to the absolute ground state. There, direct imaging and cooling schemes may be enabled by $X\,^6\Sigma^+ \rightarrow (2)\,^6\Pi$ optical transitions. Our results thus make ultracold LiCr emerge as an appealing system for a wealth of fundamental studies and future applications.

A high phase-space density sample of ^{6}Li^{53}Cr Feshbach dimers, already realized, opens exciting new routes for the investigation of strongly correlated fermionic matter. Extending the protocols developed in this work may allow us to Bose-condense Feshbach dimers—thereby paving the way to BCS-BEC crossover studies in the presence of a large mass asymmetry [75–77]. The creation of long-lived LiCr dimers in the presence of a controlled amount of Cr is a fundamental step towards novel few- and many-body phenomena, uniquely enabled by the peculiar mass ratio of our atomic Fermi mixture [37]: for instance, the existence of $LiCr_2$ fermionic trimers [78–80], and $LiCr_3$ bosonic tetramers [81–83], the emergence of new types of quasiparticles within the light-impurity problem [84,85], and, possibly, the appearance of many-body regimes beyond the BCS-BEC crossover scenario, such as trimer Fermi gases [86] or quartet superfluid states [87].

Our joint experimental and theoretical results suggest that the realization of quantum gases of doubly polar ^{6}Li^{53}Cr bosonic molecules, with large electric and magnetic dipole moments, is within reach. Clearly, identification of the optimal STIRAP transfer will require extensive laser spectroscopy, but this will be greatly facilitated by our *ab initio* model predictions and by the long lifetime of Feshbach dimers, already achieved. Interestingly, electric dipole moments as high as 1 D can already be obtained in relatively shallow vibrational levels of LiCr with $v \simeq 37$ and a binding energy as low as 190 cm^{-1}; see Sec. VI. Given the relatively simple spectroscopic survey needed to find these states, this possibility represents an appealing intermediate, short-term step. In particular, such vibrationally excited molecules offer high sensitivity to the electron-to-proton mass ratio m_e/m_p [69], overcoming that of alkali and alkaline-earth dimers, and they could be employed to detect possible variations of m_e/m_p in precision measurements, and to gain insight into fundamental physics.

LiCr molecules, pinned in optical lattice sites or tweezer traps, will find immediate application in the context of quantum simulation of spin Hamiltonians [4–7], as well as high-dimensional quantum computing [8,9], exploiting the internal spin degree of freedom, absent in ground-state alkali dimers. Bulk gases will be ideal test beds for quantum controlled chemistry: although ground-state LiCr molecules are chemically unstable under atom-exchange reactions $LiCr + LiCr \rightarrow Li_2 + Cr_2$, in their spin-stretched state resulting from STIRAP they are expected to be stabilized because the decay to deep Cr_2 levels becomes spin forbidden. The predicted rotational constant and electric dipole moment, incidentally close to those of CaF, suggest that collision shielding, via microwave [88] or static electric fields [89,90], could be applied to stabilize bulk samples and perform evaporative cooling. Additionally, resonant tuning of magnetic [12] and field-linked resonances [91] may be investigated in LiCr. Prospects for precision measurements also appear promising: on top of the measurement of m_e/m_p already mentioned, the observation of the electron's electric dipole moment may be facilitated by the internal comagnetometer states offered by long-lived $^4\Delta$ metastable levels [71], unavailable in alkali-metal dimers.

Finally, it is worth noting that fermionic isotopologues ^{7}Li^{53}Cr and ^{6}Li^{52}Cr could also be formed via magnetoassociation across suitable FRs [29] on our experimental setup. More generally, combining Cr with other alkalis, with heavier mass and lower electronegativity than Li, could result in molecular paramagnetic species with even larger electric dipole moments.

ACKNOWLEDGMENTS

We thank A. Canali, R. Grimm, S. Meek, D. Petrov, G. Santambrogio, and the LENS Quantum Gases group for fruitful discussions, and G. Rosi and L. Salvi for technical

support. We also acknowledge A. Canali for contributions to the experiment, and D. Petrov for sharing unpublished theoretical results. K.Z.-K., M.G. and M.T. acknowledge Poland's high-performance computing infrastructure PLGrid (HPC Center: ACK Cyfronet AGH) for providing computer facilities and support (computational Grant No. PLG/2023/016115).

This work was supported by the European Research Council under Grant No. 637738, by the EU H2020 Marie Skłodowska-Curie under Grant No. 894442 (CriLiN; fellowship to A.C.), by the National Science Center, Poland under Grants No. 2019/35/N/ST4/04504 and No. 2020/38/E/ST2/00564, by the Italian Ministry of University and Research under PRIN2022 Project No. 20227F5W4N, and, cofunded by the European Union—NextGenerationEU, under the "Integrated infrastructure initiative in Photonic and Quantum Sciences" (I-PHOQS; CUP B53C22001750006), the PE0000023-NQSTI project, and the Young Researcher Grants No. MSCA_0000042 (PoPaMol; fellowship to A.C.) and No. MSCA_0000048 (MajorSuperQ; fellowship to M.S.).

APPENDIX A: TRAP CONFIGURATION AND SAMPLE CONDITIONS

The BODT used in this work is realized by superimposing an infrared laser beam with a green one, both propagating along the x direction in the horizontal (x,y) plane [28]. The former is delivered by a multimode 1070-nm fiber laser (IPG Photonics YLR-300) and has a horizontal (vertical) waist of $w_y = 58$ μm ($w_z = 44$ μm). The latter is generated by a single-mode source at 532 nm (Lighthouse Photonics Sprout-G) and has a horizontal (vertical) waist of $w_y = 48$ μm ($w_z = 45$ μm). The 1560-nm FORT employed to obtain long-lived molecular samples (see Sec. V) has a circular beam waist of 55 μm, and it is delivered by an erbium fiber amplifier (Keopsys-CEFA-C-BO-HP) seeded by a single-mode master laser (Rock™, NP Photonics).

Our magnetic field coils provide, besides the required bias, both a magnetic field curvature in the (x,y) horizontal plane of 12.3 G cm^{-2}—which determines the axial confinement along the weak axis of the BODT—as well as a magnetic field gradient of about 1.5 G cm^{-1} along the vertical direction. The latter value is optimized in order to levitate the heavier Cr atoms—that would otherwise be lost from the trap at the end of the evaporation stage—and, simultaneously, to minimize the gravitational sag between the two mixture components.

Typical trap frequencies for most of the experimental studies described in the main text are $(\nu_x,\nu_y,\nu_z) = (17,115,156)$ Hz and $(\nu_x,\nu_y,\nu_z) = (14,124,118)$ Hz for Li and Cr, respectively, with an overall trap depth ratio of $U_{\mathrm{Li}}/U_{\mathrm{Cr}} = 0.75$, which can be tuned thanks to the species-dependent dynamic polarizabilities [56] of the two BODT beams.

To optimize magnetoassociation, we maximize the spatial density overlap between Li and Cr clouds by tuning the power ratio of the BODT. We do this by linearly ramping the green ODT from the final evaporation value, which provides a deeper trap for Cr with respect to Li, to a lower value right before the magnetoassociation field sweep. During this ramp the trap gets tighter and deeper for Li, while the opposite holds for Cr. A sweet spot exists for a green-to-IR power ratio of about 0.35, which corresponds to $P_{\mathrm{G}} = 60$ mW and $P_{\mathrm{IR}} = 180$ mW, where $\langle n_{\mathrm{Li}} n_{\mathrm{Cr}}\rangle = 5.0(5)\times 10^{16}$ cm^{-3}. The confinement in this BODT configuration is characterized by geometrically averaged radial trapping frequencies $\sqrt{\nu_y\nu_z}$ of about 340, 105, and 145 Hz for Li, Cr, and LiCr dimers, respectively. The axial confinement, as already mentioned above, is entirely set by our magnetic field curvature, and it is characterized by trapping frequencies of $\nu_{x,\mathrm{Li}} = 17.0(6)$ Hz, $\nu_{x,\mathrm{Cr}} = 14.0(5)$ Hz, and $\nu_{x,\mathrm{LiCr}} = 12.1(5)$ Hz, where the LiCr molecules are assumed to be fully closed channel. After the BODT is switched off, atoms and molecules expand into a magnetic saddle potential, with trapping frequencies $\nu_x = \nu_y$ in the horizontal plane—equal to the *in situ* axial ones—and vertical antitrapping frequencies of $\nu_z = i\sqrt{2}\nu_x$.

APPENDIX B: MAGNETIC FIELD STABILITY

The experimental studies described in the main text require excellent stability of the magnetic field bias, and an accurate dynamic tuning of it within the experimental cycle, in light of the comparatively narrow width of the available Li-Cr FRs combined with their high-field location, exceeding 1.4 kG. In our setup, a highly stable magnetic field is produced by means of three different sets of coils, denoted FESH1, FESH2, and COMP coils, respectively. The main FESH1 coils are able to produce magnetic fields of up to 1.5 kG, corresponding to a dc current of about 200 A. This is generated by a 15-kW programmable power supply (TDK-Lambda GSP-80-195). The FESH1 current, measured with a current transducer (LEM ITN 600-S ULTRASTAB), is actively stabilized via a proportional-integral controller acting on the voltage programming input of the power supply. This ensures reproducibility and medium-term stability of the applied bias field. The (much smaller) FESH2 coils can produce fields of about 2.5 G at the maximum employed current of 5 A. They are used, in combination with FESH1, to finely tune the magnetic field around the FR. The FESH2 current is also actively stabilized by means of a similar setup as the FESH1 current with a second controller and current transducer set of the same type. As far as the FESH2 setup is concerned, active stabilization of the current allows us to

reduce the noise of the generated magnetic field well below 1 mG.

The FESH1 coils, instead, that are driven with a significantly higher current, exhibit a larger residual closed-loop noise synchronous with the 50-Hz mains. This is characterized by a peak-to-peak amplitude of about 40 mG at 1.4 kG and by Fourier components at 50 Hz and a few higher harmonics; see the blue squares and blue curve in Fig. 13. This behavior is revealed by synchronizing the experimental sequence with the 50-Hz mains. Since the line carrier frequency can vary appreciably within the duration of the experiment, we not only synchronize the start of the experiment with the ac line, but also before the execution of field-sensitive measurements. This allows us to trace the magnetic field fluctuations at $t \geq t_1$ via rf spectroscopy on the $\mathrm{Cr}|1\rangle \leftrightarrow \mathrm{Cr}|2\rangle$ Zeeman transition. Specifically, we adjust the rf power and pulse duration to achieve a π pulse on resonance, and then detune the frequency to yield a 50% transferred fraction. This side-of-fringe configuration yields the maximum sensitivity to magnetic field variations and, for Fourier-limited pulse widths exceeding noise-induced frequency shifts, it can be used to unambiguously retrieve the time evolution from the transfer efficiency. For this reason, we initially employ a 1.8-ms-long pulse to characterize the noise of our coil setup, and only at a later stage we extend it to 3.6 ms to gain in sensitivity at the expense of a reduced bandwidth. A typical magnetic field trace obtained with the initial 1.8-ms-long pulse is presented in Fig. 13 (blue squares). As anticipated, the observed trend is well fitted by a sum of sinusoidal functions with a main 50-Hz component and a few higher harmonics of progressively smaller amplitudes; see the solid blue line. The best-fit function to the experimental data is then reversed and used to drive the additional COMP coil setup to implement the feed forward to compensate field fluctuations. A second iteration with the 3.6-ms-long pulse allows us to further refine the signal sent to the COMP coils. Through this active compensation procedure, we are finally left with residual 5-mG peak-to-peak fluctuations synchronous with the 50-Hz mains; see the green circles in Fig. 13. Such a stability is found to be maintained over several weeks.

In order to determine the shot-to-shot noise of the magnetic field, we acquire statistics of the observed transfer efficiency for variable spectral resolution at fixed time of the pulse t_1 during the sequence. The standard deviation of the samples is linearly correlated with the spectral resolution over a wide range and can be interpreted as shot-to-shot standard deviation of about 2.5 mG, which constitutes the main source for field fluctuations asynchronous with the 50-Hz mains. Finally, slow thermal effects on the whole coil setup cause a linear drift of the bias field of about 4 mG/h, which we compensate for by finely adjusting the FESH2 coil current.

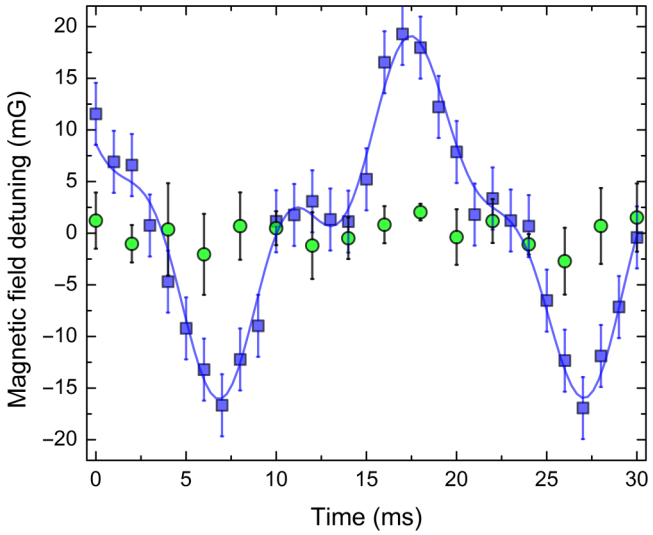

FIG. 13. Stability of the bias magnetic field at 1.4 kG. Blue squares show a typical magnetic field trace, obtained through the spectroscopic technique described in the text after synchronizing the experimental sequence with the 50-Hz mains, once the sole active stabilization of the current of the FESH1 and FESH2 coil setups is implemented. The observed trace, synchronous with the mains and characterized by a peak-to-peak amplitude of about 40 mG, is well fitted to a sum of sinusoidal functions with a main Fourier component at 50 Hz plus a few higher harmonics of decreasing amplitude (blue line). Employing the (reversed) fitted trace to drive the COMP coil setup, we remove the main (synchronous) noise contribution, being left with only a residual asynchronous noise (green circles), characterized by a standard deviation of about 2.5 mG.

APPENDIX C: ELASTIC COLLISIONS

1. The coupled oscillator model

The c.m. dynamics of the lithium and chromium cloud, explored throughout different interaction regimes, as described in Sec. II, is analyzed in terms of a well-established model of two coupled oscillators, already tested on both homo- and heteronuclear atomic mixtures [32–35]. In this framework, the c.m. evolution of the two clouds along the axial (x) direction is described by two coupled differential equations that we express as

$$\begin{aligned} m_{\mathrm{Cr}}\ddot{x}_{\mathrm{Cr}} &= -m_{\mathrm{Cr}}\omega_{\mathrm{Cr}}^2 x_{\mathrm{Cr}} - \frac{4m}{3}\gamma_{\mathrm{el}}(\dot{x}_{\mathrm{Cr}} - \dot{x}_{\mathrm{Li}}), \\ m_{\mathrm{Li}}\ddot{x}_{\mathrm{Li}} &= -m_{\mathrm{Li}}\omega_{\mathrm{Li}}^2 x_{\mathrm{Li}} - \frac{4mN_{\mathrm{Cr}}}{3N_{\mathrm{Li}}}\gamma_{\mathrm{el}}(\dot{x}_{\mathrm{Li}} - \dot{x}_{\mathrm{Cr}}). \end{aligned} \tag{C1}$$

Here $\omega_{\mathrm{Cr(Li)}}$ and $N_{\mathrm{Cr(Li)}}$ denote the Cr (Li) axial trap frequency and atom number, respectively, and $m = m_{\mathrm{Li}}m_{\mathrm{Cr}}/(m_{\mathrm{Li}} + m_{\mathrm{Cr}})$ is the Li-Cr reduced mass. The sloshing dynamics of the two clouds are coupled through the rightmost damping terms in Eqs. (C1). The damping rates scale with the mean number of elastic Li-Cr collisions per unit of time experienced by each component, and are

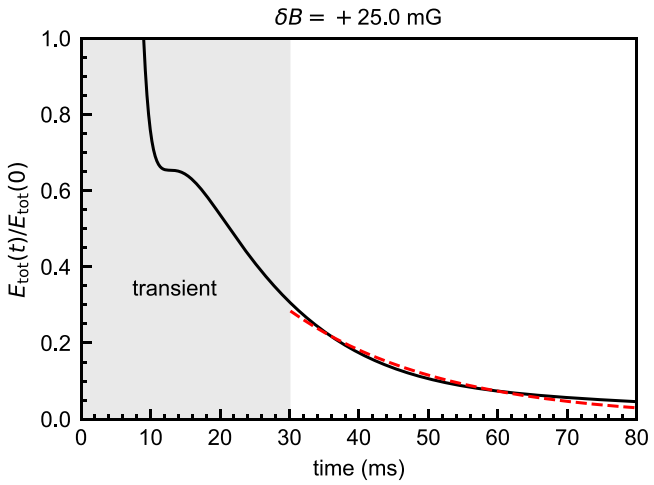

FIG. 14. Time evolution of the total energy, extracted from the fits of Eqs. (C1) to the data, characterized by an initial transient behavior, and a subsequent almost pure exponential decay. Here, E_{tot} is shown for $\delta B = 25$ mG (black solid line), corresponding to $\gamma_{el} = 490$ Hz. The red dashed line is the fitted exponential decay after the transient behavior.

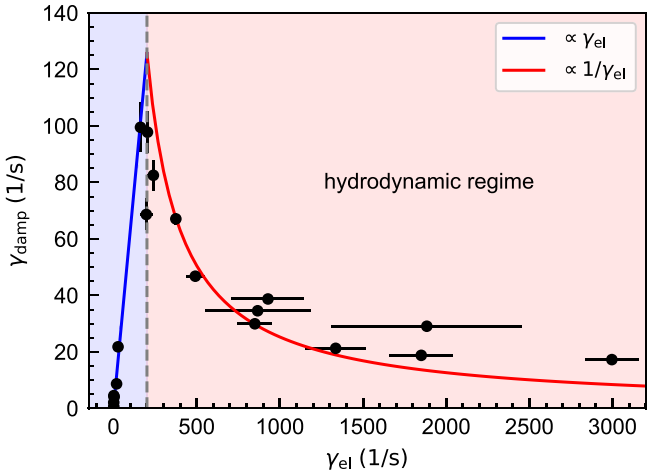

FIG. 15. Identification of the transition from the collisionless to the collisionally hydrodynamic regime via the analysis of the damping rate γ_{damp} as a function of γ_{el}: a scaling of $\gamma_{damp} \propto \gamma_{el}$ is visible in the collisionless regime (blue line and shaded region), while a scaling $\propto 1/\gamma_{el}$ characterizes the hydrodynamic regime (red line and shaded region). Both lines are guides to the eye.

here expressed in terms of the scattering rate per minority Cr atom γ_{el}. By fixing the axial frequencies and initial conditions $[x_i(0), \dot{x}_i(0)]$ for $i = \mathrm{Li}, \mathrm{Cr}$ to their experimentally determined values, and accounting for the measured atom number evolution, we fit Eqs. (C1) to the recorded oscillation dynamics—see the examples in the right panels of Fig. 2(b)—and thus extract γ_{el} as the sole free fitting parameter. The experimentally determined Cr collision rate is compared in Fig. 2(c) with the theory expectation [92] that we evaluate as

$$\gamma_{el} = \langle n_{Li} \rangle_{Cr} \langle \sigma(a, R^*, k) \times v \rangle_T, \tag{C2}$$

where $\langle n_{Li} \rangle_{Cr} = \int n_{Li}(\mathbf{r}) n_{Cr}(\mathbf{r}) d\mathbf{r} / N_{Cr}$ denotes the lithium density averaged over the chromium one, $\hbar k$ is the relative momentum for Li-Cr collisions, and $v = \hbar k/m$ is the corresponding relative velocity. Here $\sigma(a, R^*, k)$ represents the (field- and momentum-dependent) elastic cross section and $\langle \cdot \rangle_T$ indicates thermal averaging over all relative momenta. To a good approximation, $\langle n_{Li} \rangle_{Cr}$ remains constant to the experimentally determined value of 1.2×10^{11} cm^{-3} at all detunings and evolution times, given the moderate atom loss of the Li majority component. The elastic cross section is given by (see, e.g., Ref. [37])

$$\sigma(a, R^*, k) = \frac{4\pi a^2}{[1 + (ka)^2 R^*/a]^2 + (ka)^2}, \tag{C3}$$

where $R^* = 6000 a_0$ and $a(\delta B) = a_{bg}(1 - \Delta B/\delta B)$, with $a_{bg} = 41.48 a_0$ and $\Delta B = 0.48$ G for our FRs. For simplicity of the calculation, thermal averaging of $\langle \sigma(a, R^*, k) k \rangle_T$ is performed by neglecting the Cr thermal distribution within the momentum integral. This is justified by the fact that, owing to the large mass imbalance of our mixture, $m_{Cr}/m_{Li} \simeq 8.8$, the Li-Cr relative velocity is essentially set by the sole lithium one. Under this approximation, averaging over a Fermi-Dirac distribution at $T/T_F \sim 0.3$, or over a Boltzmann-gas weight at an effective temperature of $T = 700$ nK, yields nearly identical results throughout the interaction regime we explored. We employ Eq. (C2) to fit the experimental data, with the resonance pole position B_0 as the single free parameter implicitly entering Eq. (C3), while fixing all other quantities to the corresponding values experimentally determined or given by the quantum collisional model we developed in Ref. [29]. We remark how our sizable R^* parameter ensures that the maximum of the cross section (C3)—where $\sigma = 4\pi/k^2$—is reached at a large but finite scattering length, $a < 0$, for which $1/a + R^* k^2 = 0$ [37]. This feature, which also persists after thermal averaging [see Eq. (C2)], causes the maximum of γ_{el} to occur at a small $\delta B > 0$ value, as visible in Fig. 2(c).

2. Transition from the collisionless to the collisionally hydrodynamic regime

Previous studies [32–35] identified the transition from the collisionless to the hydrodynamic regimes by analyzing the scaling of the damping rate γ_{damp} of the coupled oscillations with respect to the collision rate γ_{el}. Specifically, in the collisionless regime γ_{damp} linearly grows with γ_{el}, whereas in the hydrodynamic regime it exhibits a progressive reduction proportional to $1/\gamma_{el}$.

Extracting γ_{damp} from a fit to the c.m. dynamics is rather challenging, owing to the concurrent oscillatory motion, especially when considering the initial short-time evolu-

tion near the resonantly interacting region; see the example of Fig. 2(b) at $\delta B = 30$ mG.

A convenient way to extract the damping rates at all detunings, given our limited observation time over a few oscillation periods, is to employ the fitted $x_{\mathrm{Li}}(t)$ and $x_{\mathrm{Cr}}(t)$ to obtain the total energy $E_{\mathrm{tot}}(t) = E_{\mathrm{kin}}(t) + E_{\mathrm{pot}}(t)$, with $E_{\mathrm{kin}} = \frac{1}{2}(m_{\mathrm{Li}}\dot{x}_{\mathrm{Li}}^2 + m_{\mathrm{Cr}}\dot{x}_{\mathrm{Cr}}^2)$ and $E_{\mathrm{pot}} = \frac{1}{2}(m_{\mathrm{Li}}\omega_{\mathrm{Li}}^2 x_{\mathrm{Li}}^2 + m_{\mathrm{Cr}}\omega_{\mathrm{Cr}}^2 x_{\mathrm{Cr}}^2)$. As shown in the example in Fig. 14, the evolution of $E_{\mathrm{tot}}(t)$ (black line) is in fact less affected by the oscillatory dynamics, such that a damping rate can be more easily extracted. Indeed, after an initial, short transient time of about 30 ms, excluded from the fit, $E_{\mathrm{tot}}(t)$ exhibits a clean decay that is fitted by an exponential decaying function (red dashed line), from which we obtain γ_{damp} at all detunings. In Fig. 15 we present the extracted damping rate γ_{damp}, plotted as a function of the experimentally determined γ_{el}. The observed trend is indeed found to follow the expected transition from collisionless to collisional hydrodynamics scaling [32–35], approximately once γ_{el} starts exceeding the axial trapping frequencies of the two atomic

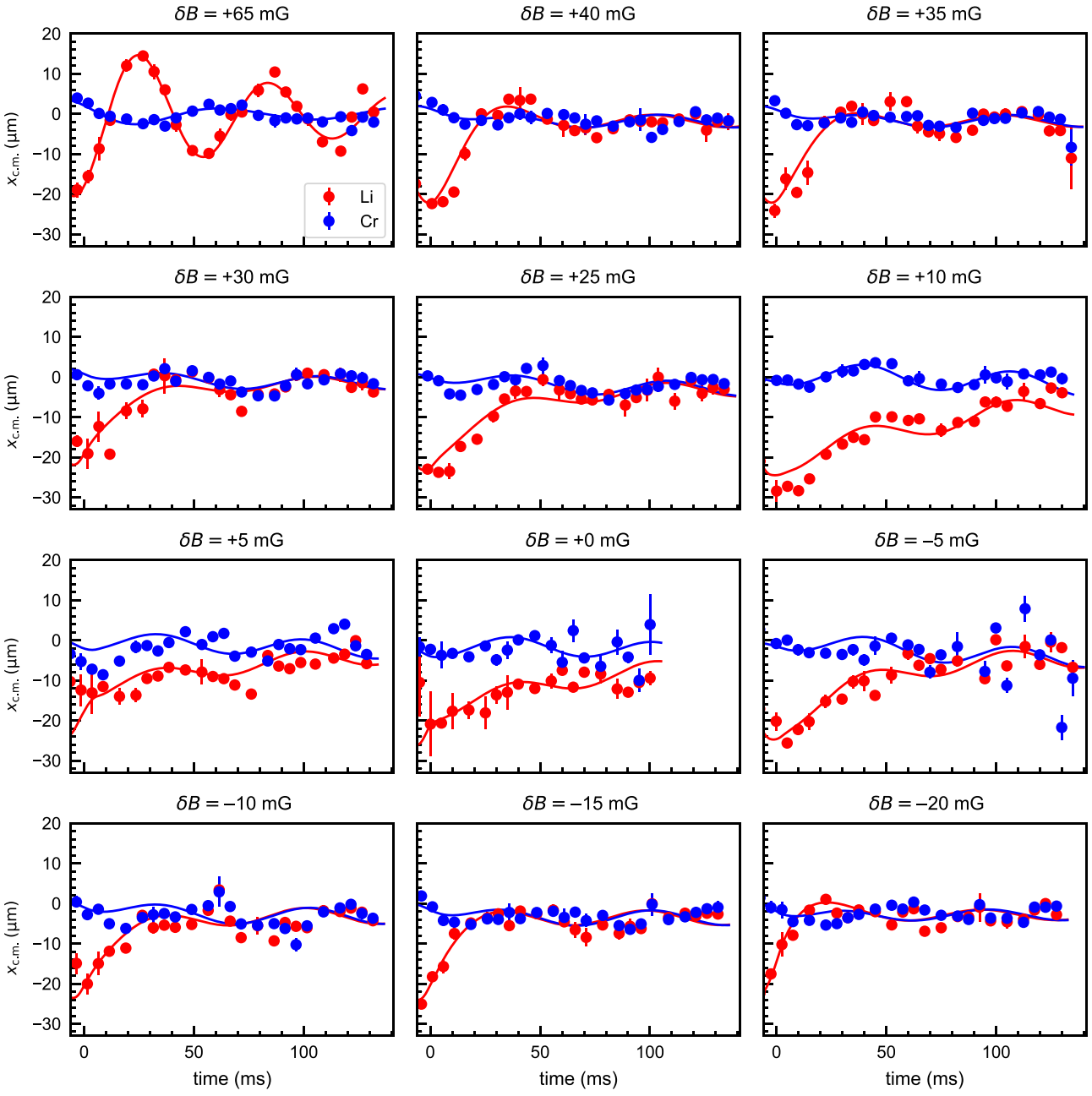

FIG. 16. Examples of in-trap oscillations of Li and Cr centers of mass, recorded for different detuning δB across the FR region, together with the fitted coupled oscillator model equations (C1) (solid lines).

components. For our experimental conditions, this happens for magnetic field detunings $\delta B \leq 30$ mG, below which, as shown by the data presented in Fig. 16, a rapid phase locking of the two c.m. dynamics is observed and, correspondingly, $\gamma_{\rm damp}$ is strongly reduced. We emphasize that this observation indicates our experimental capability to access the hydrodynamic regime not only along the weak, axial direction of our trap, but, once $\gamma_{\rm el} > \omega_{y,z}$, also along the transverse ones.

APPENDIX D: THREE-BODY RATE COEFFICIENT AND FR POLE

In order to further characterize the stability of the atomic mixture in the strongly interacting region, as well as to pinpoint the (absolute) magnetic field location B_0 of the FR pole, we have performed additional studies of inelastic three-body recombination processes, besides those described in Sec. II. While such a survey has been conducted for each of the four high-field FRs occurring in all Li$|i\rangle$-Cr$|j\rangle$ combinations with $i,j = 1, 2$ [29], in the following we summarize our experimental procedures and findings by focusing on the absolute ground-state mixture Li$|1\rangle$-Cr$|1\rangle$, and on the associated FR at 1414 G. Conceptually, this additional characterization is based on protocols and analysis closely following those already discussed in Sec. II to extract $\gamma_{\rm loss}$: after preparing a weakly interacting mixture at a large and positive detuning from the FR pole, we quickly ramp the magnetic field towards the resonance region at small, variable δB values, at which we monitor the subsequent atom number decay $N_{\rm Cr}(t)$ of the Cr minority component as a function of time, evolving according to $\dot{N}_{\rm Cr} = -K_3\langle n_{\rm Li}^2\rangle N_{\rm Cr} = -\gamma_{\rm loss} N_{\rm Cr}$. Each magnetic field bias investigated is calibrated against the Li$|1\rangle \leftrightarrow$ Li$|2\rangle$ rf transition, both before and after each decay measurement.

Contrarily to Sec. II, however, here we opt to investigate steady mixtures—i.e., not exhibiting in-trap sloshing dynamics—that are prepared within our BODT trap, rather than in the sole IR beam. On the one hand, this allows, at each magnetic field value, for a more accurate determination of the mean squared Li density $\langle n_{\rm Li}^2\rangle_{\rm Cr}$, now constant over time. This, combined with the $\gamma_{\rm loss}$ values extracted from exponential fits to the Cr atom number evolution, as for the Sec. II measurement, allows us to obtain, at each bias field, the three-body rate coefficient for the dominant Li-Li-Cr recombination processes as $K_3 = \gamma_{\rm loss}/\langle n_{\rm Li}^2\rangle_{\rm Cr}$. On the other hand, exploitation of the green beam of our BODT, on top of the IR one, allows for an alternative, precise detection of the FR pole location B_0: indeed, even a relatively low power level of the green light is found to induce strong photoexcitation losses once LiCr Feshbach dimers are formed; see Appendix F. As such, once the magnetic field is lowered below B_0 on the molecular side of the FR, this light-induced, strong decay channel is opened, and it greatly overcomes the three-body collisional one. When this happens, the sample lifetime is markedly reduced, hence yielding an enhanced $\gamma_{\rm loss}$. This experimental protocol thus allows us to accurately determine both the three-body recombination rate coefficient K_3 for $B \geq B_0$, as well as to obtain an additional measure of the FR pole B_0—besides that obtained from the fit of $\gamma_{\rm el}$ presented in Sec. II—solely based on the study of inelastic losses.

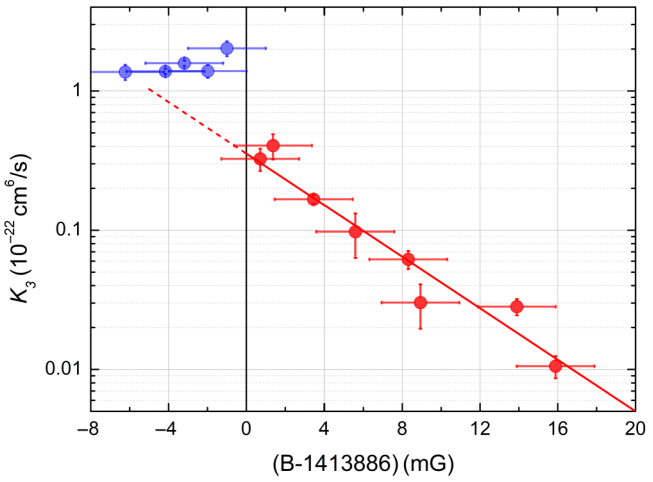

FIG. 17. Three-body recombination rate coefficient for Li-Li-Cr collisions as a function of magnetic field across the FR region, obtained for mixtures prepared in the BODT trap by following the analysis described in the text. Strong photoexcitation losses, induced by the green light of our trap for $\delta B \leq 0$, results in a sharp increase of the derived K_3, marked by the different color of the experimental data. This enables us to pinpoint the absolute resonance pole position B_0 with a 5-mG accuracy; see the text and Table I. Red line is the best fit of the data above the FR pole to Eq. (D1), fixing $\delta\tilde{\mu} = 0.77 \times 2\mu_B$ while leaving both T and K_3^0 as free parameters.

The results of this characterization are summarized in Fig. 17, where we show the experimentally determined K_3 coefficient as a function of the magnetic field across the resonance region. We interpret the sudden jump between the red and blue data points as the crossing of the resonance pole, below which Feshbach dimers are formed and quickly lost due to the fast trap-induced photoexcitation process; see Appendix F. The jump is centered at $B_0 = 1413.886(5)$ G, and the error budget accounts for residual ac field noise, calibration of the COMP coils, magnetic field inhomogeneity, and residual long-term drifts, in order of importance. Experimental data marked in blue can no longer be interpreted as a K_3 coefficient for three-body collisions and their interpretation goes beyond the scope of our work. At positive detunings (i.e., for $B > B_0$), and similarly to the $\gamma_{\rm loss}$ trend presented in Sec. II, the extracted K_3 exhibits an exponential growth as the resonance pole is approached from above, $\delta B \to 0^+$, in qualitative agreement with previous observation

TABLE I. Precise determination, through loss-spectroscopy measures in the BODT, of the magnetic field location of the high-field s-wave Feshbach resonances for all Li$|i\rangle$-Cr$|j\rangle$ combinations with $i,j = 1, 2$, already identified in Ref. [29] with lower accuracy. Error budget, in brackets, accounts for residual ac field noise, calibration of the COMP coils, magnetic field inhomogeneity, and residual long-term drifts, in order of importance.

	Cr$\|1\rangle$	Cr$\|2\rangle$
Li$\|1\rangle$	1413.886(5)	1417.937(30)
Li$\|2\rangle$	1460.933(5)	1464.159(30)

on homonuclear Fermi mixtures near narrow Feshbach resonances [36].

Following the theoretical analysis of Ref. [36], valid for an infinitely narrow FR ($R^* \to \infty$), the K_3 coefficient for a thermal mixture is expected to vary, for $\delta B \geq 0$, as

$$K_3(\delta B, T) = K_3^0(T) \exp\left(-\frac{\delta\mu \delta B}{k_B T}\right). \tag{D1}$$

Here $K_3^0(T)$ is the (temperature-dependent) maximum value of K_3 reached at the resonance pole, $\delta\mu$ is the differential magnetic moment between the open and closed channels associated with the FR, T is the gas temperature, and k_B is the Boltzmann constant. In the case of degenerate samples, one can still employ Eq. (D1) by defining an effective temperature $T_{\rm eff}$ that connects with the mean kinetic energy of the system. In our case, this is essentially set by the majority Li Fermi gas, such that we evaluate $T_{\rm eff}$ by setting $3/2 k_B T_{\rm eff} = \langle E_{\rm kin,Li}(T/T_F)\rangle$. Taking the experimentally determined value of $T/T_F = 0.27(2)$, with $T_F = 1.25(5)$ μK, and considering that, for an ideal Fermi gas, $\langle E_{\rm kin,Li}(0.27)\rangle \sim 0.55 k_B T_F$, we obtain $T_{\rm eff} \sim 460$ nK.

However, by fixing $T_{\rm eff}$ to this value and setting the magnetic moment to $\delta\mu = 2\mu_B$, i.e., to the value characterizing each of the high-field FRs of Li-Cr [29], Eq. (D1) yields a trend significantly steeper than that experimentally determined. Interestingly, this mismatch arises from the fact that our resonance is indeed not infinitely narrow, featuring a sizable though finite R^* value. Extension of the theory of Ref. [36] to finite effective-range values (D. Petrov, unpublished) yields a trend for K_3 qualitatively analogous to that of Eq. (D1), but with an effective magnetic moment $\delta\tilde{\mu}$ that is progressively decreased for decreasing R^* values. In particular, such an extended theory model predicts, for the Li-Cr FRs here investigated, featuring $R^* \sim 6000 a_0$, a $\delta\tilde{\mu} = 0.77\delta\mu$. A functional fit of Eq. (D1) to the red dataset in Fig. 17, where we set $\delta\tilde{\mu} = 0.77 \times 2\mu_B$ while leaving both T and K_3^0 as free parameters, is plotted in the figure as a solid red line. The fit, which reproduces our data remarkably well, returns $K_3^0 = 0.35(5) \times 10^{-22}$ cm^6 Hz and $T = 490(40)$ nK, the latter matching within uncertainty the estimated $T_{\rm eff}$ value. A fit based on the same extended theory model is employed to analyze the $\gamma_{\rm loss}$ data shown in Fig. 2(c) of Sec. II. Similar protocols were employed to pinpoint the pole of all four FRs occurring between the two lowest spin states of Li and Cr at high fields, and the results of this characterization are summarized in Table I.

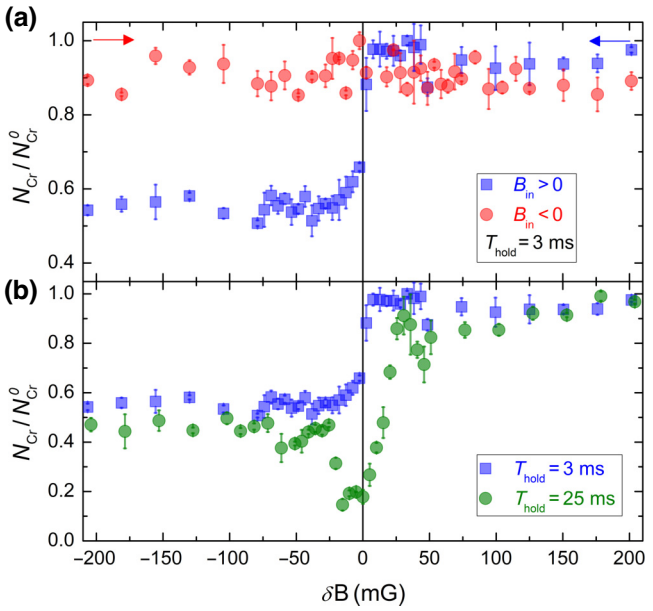

FIG. 18. (a) Fractional Cr loss measured in the BODT as a function of the magnetic field detuning that is reached through a ramp starting at a bias field $B_{\rm in}$ either far above (blue squares) or far below (red circles) the FR pole. The signal is detected after a hold time at the final field of 3 ms. (b) Comparison of the Cr loss line shapes, obtained with magnetic field ramps starting from $B_{\rm in} > 0$, and measured after a hold time $T_{\rm hold} = 3$ ms (blue squares) and $T_{\rm hold} = 25$ ms (green circles).

Finally, we remark how the strong photoexcitation loss induced by the green BODT beam represents a valuable tool to monitor molecule formation through negative signals at short hold times $T_{\rm hold}$, unaffected by spurious offset induced by three-body loss processes. This is demonstrated by the data presented in Fig. 18(a). There, we show the Cr loss signals measured at $T_{\rm hold} = 3$ ms as a function of the final detuning, which is reached through magnetic field ramps starting either far above ($B_{\rm in} > 0$, blue squares) or far below ($B_{\rm in} < 0$, red circles) the FR pole. In the former configuration—that allows for magnetoassociation of LiCr dimers—we reveal a strong drop of the Cr signal as the FR pole is crossed. In contrast, in the latter case—for which molecule formation can only occur via three-body processes, and only collisional losses may reduce the signal—the Cr population remains constant within experimental noise throughout the resonance region. It is thus legitimate to attribute the observed drop of the blue data solely to molecule formation via magnetoassociation, since spurious effects due to three-body

processes are negligible at short $T_{\rm hold}$ values. Indeed, collisional losses, which add to those induced by photoexcitation of LiCr dimers, become sizable only at significantly longer hold times. This is testified by Fig. 18(b), where the magnetoassociation line shape obtained with $T_{\rm hold} = 3$ ms (blue squares), and already shown in Fig. 18(a), is compared with that measured after a hold time of 25 ms (green circles). As one can see, only for such long $T_{\rm hold}$ values three-body losses start yielding, near the resonance pole, a signal contribution comparable with that due to molecule formation.

APPENDIX E: PROBING FESHBACH DIMER PROPERTIES THROUGH ABSORPTION IMAGING ON ATOMIC TRANSITIONS

In the following we provide further details on the model introduced in Sec. IV B, and on the data analysis that allows us to determine both open-channel fraction and binding energy of LiCr dimers through absorption images acquired with laser light resonant with atomic transitions. As explained in Sec. IV B, we assume that the atomic light interacts with Feshbach dimers only via a non-negligible open-channel fraction $1 - Z$ [assumption (i)], that the dimer dissociation rate follows Fermi's golden rule $\gamma_b = \gamma_a(1 - Z)$ [assumption (ii)], and, finally, that the imaging is performed on a cycling transition with low saturation parameter $s_a \ll 1$ [assumption (iii)]. In this case the instantaneous optical density of the initially pure molecular sample can be written [see Eq. (7)] as

$$\mathrm{OD}(t) = \mathrm{OD}_a(1 - e^{-\gamma_b t}).$$

Here OD_a is the optical density of an atomic sample of equivalent column density $\mathrm{OD}_a = \sigma_a n^0_{2D,b}$, with σ_a being the field-dependent absorption cross section and $n^0_{2D,b}$ the molecule column density.

We now derive the observed optical density after an absorption imaging pulse of duration τ_p from the instantaneous time-dependent optical density $\mathrm{OD}(t)$ above. We recall that the temporal variation of photon counts N_p on the camera during the probe pulse shining onto the Feshbach molecule sample follows the relation

$$\partial_t N_{p,b} = C \times I_0 \times e^{-\mathrm{OD}(t)}, \tag{E1}$$

where C is the overall quantum efficiency of the imaging system and I_0 is the laser intensity. At the end of the pulse, then, we have

$$N_{p,b}(\tau_p) = CI_0 e^{-\mathrm{OD}_a} \int_0^{\tau_p} e^{\mathrm{OD}_a e^{-\gamma_b t}} dt, \tag{E2}$$

in contrast with the case of a pure atomic sample, for which $N_{p,a}(\tau_p) = CI_0\tau_p e^{-\mathrm{OD}_a}$. In both cases, the reference image, with neither dimers nor atoms, yields $N^0_{p,b} = CI_0\tau_p$ counts. Using the definition of optical density $\mathrm{OD} = -\ln(N_p/N^0_p)$, taking as reference the atomic optical density at resonance OD^0_a, we derive the suppression factor

$$\frac{\overline{\mathrm{OD}}(\tau_p)}{\mathrm{OD}^0_a} = \frac{\gamma_a}{\gamma^0_a}\left[1 - \frac{1}{\mathrm{OD}_a}\ln\left(\frac{1}{\tau_p}\int_0^{\tau_p} e^{\mathrm{OD}_a e^{-\gamma_b t}} dt\right)\right], \tag{E3}$$

$$\gamma^0_a = \gamma(s_a, \Gamma_a, 0), \tag{E4}$$

$$\gamma_b = \gamma_a(s_a, \Gamma_a, \delta_a + \epsilon_b/h)(1 - Z), \tag{E5}$$

where the B-field dependence of Z, δ_a, and ϵ_b is implicit. In our case we have $\delta_a(B) = \mu_B \delta B$ for the Zeeman shifts of the imaging transitions of both Li and Cr. In the limit of low optical density, $\mathrm{OD}^0_a \ll 1$, Eq. (E3) simplifies to Eq. (8).

Most importantly, our model can be exploited to extract the open-channel fraction at any detuning, without *a priori* knowledge of the functional forms of $Z(\delta B)$ and $\epsilon_b(\delta B)$. As long as the binding energy of the Feshbach molecule is negligible with respect to the linewidth, $\epsilon_b/h \ll \Gamma_a$, Eq. (E3) only has $Z(\delta B)$ as the unknown quantity and can easily be inverted, $N_i(\delta B_i) \to Z_i(\delta B_i)$. If this condition does not hold, we are left, at each δB_i value, with two unknown quantities Z_i and $\epsilon_{b,i}$ that cannot be uniquely inferred from N_i. To circumvent this limitation, and without loss of generality, we make use of the properties of the Feshbach state summarized by the Hellman-Feynman theorem (4) and the limiting behavior for $\delta B \to 0$ of the magnetic moment and binding energy, $\delta\mu_b \to 0$ and $\epsilon_b \to 0$, respectively. Thus, instead of extracting from each measurement point $N_i(\delta B_i) \to Z_i(\delta B_i)$, we iteratively run over consecutive measurement points starting from the largest positive detuning $\max(\delta B_i)$ and moving down to $\min(\delta B_i)$. The algorithm estimates the binding energy at δB_i as $\epsilon_{b,i} = \epsilon_{b,i-1} + Z_{i-1}\delta\mu(\delta B_{i-1} - \delta B_i)$ and extracts a new open-channel fraction $\{N_i, \epsilon_{b,i}\} \to Z_i$. The algorithm is initialized with $(Z_{i0} = 0, \epsilon_{b,i0} = 0)$ and forces $(Z_i = 0, \epsilon_{b,i} = 0)$ for all $\delta B_i > 0$.

APPENDIX F: TRAP-LIGHT-INDUCED LOSSES

The BODT configuration exploited in Sec. III to reach optimal magnetoassociation efficiency and high PSD of LiCr molecules strongly constraints the molecule lifetime on the few-millisecond timescale and is not suitable for trapping LiCr Feshbach molecules. In order to characterize this effect and decouple it from the simultaneous collisional losses, we purify the molecule sample right after molecule formation by removing the leftover atoms. $\mathrm{Li}|1\rangle$ is removed via rf pulse $\mathrm{Li}|1\rangle \to \mathrm{Li}|2\rangle$ plus optical blast, while $\mathrm{Cr}|1\rangle$ is spilled from the trap, which, for this species, is significantly shallower than for both Li and LiCr components [57].

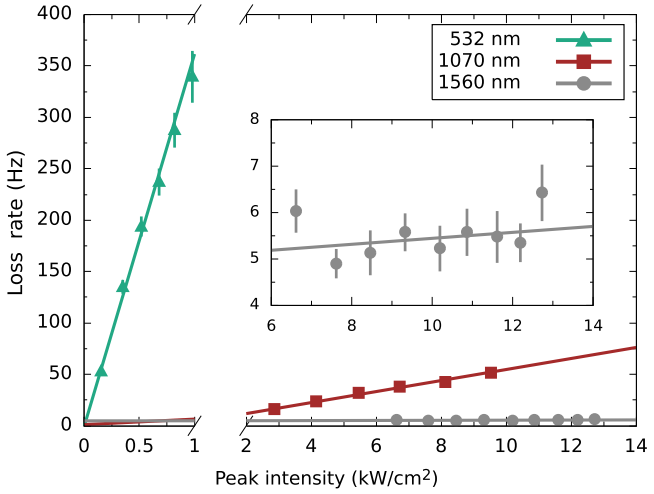

FIG. 19. Loss rates as a function of intensity for the trap wavelengths explored in this work. Green triangles, red squares, and gray circles show the experimental exponential loss rates for 532, 1070, and 1560 nm, respectively. Best linear fits to the data are plotted as solid lines with matching color code.

We first isolate the effect of the multimode 1070-nm ODT beam by ramping down the green ODT power during molecule association. We then ramp the IR power to a variable value, where we record the subsequent molecule number drop. Exponential fits to the decay data return the loss rates, which are reported as a function of the IR laser intensity in Fig. 19 (red squares) together with a linear fit to the data. Using the fitted slope and taking into account a finite open-channel fraction $1 - Z > 0$ at the probe detuning $\delta B = -100$ mG according to Ref. [24], we derive $\Gamma_{CC} = 5.9(2)$ Hz/(kW cm^{-2}). A similar analysis carried out on molecular samples realized in the 1560-nm beam yields instead a photoexcitation rate consistent with zero within experimental uncertainty; see the gray circles in Fig. 19 and corresponding inset.

Since the 532-nm green beam is antitrapping for our molecules, we study its effect by ramping it up to a variable power while keeping the IR ODT power fixed. The corresponding experimental loss rates are shown in Fig. 19 as green triangles and yield a significantly higher slope of $\Gamma_{CC} = 397(14)$ Hz/(kW cm^{-2}). This value, about 2 orders of magnitude larger than the IR one, confirms the detrimental effect of 532-nm light on Feshbach molecules and the strong constraint it puts on the possible timescale for manipulation of the LiCr sample in the combined BODT. We note that, for each dataset and trapping light, the systematic error of Γ_{CC}, arising from intraspecies LiCr-LiCr inelastic collisions, is negligible because the dimer density is kept fixed at all power levels explored within our experimental accuracy.

In conclusion of this appendix, we also remark that the measured dependence of the one-body loss rate upon the trap-light wavelength points to a stronger off-resonant photon scattering for increasing photon energy. Our findings qualitatively agree with our *ab initio* calculations, presented in Sec. VI, that find, for increasing photon energy, progressively larger transition dipole moments and higher spontaneous decay rates of molecular states coupled to the Feshbach dimer.

[1] L. D. Carr, D. DeMille, R. V. Krems, and J. Ye, Cold and ultracold molecules: Science, technology and applications, New J. Phys. **11**, 055049 (2009).

[2] M. A. Baranov, M. Dalmonte, G. Pupillo, and P. Zoller, Condensed matter theory of dipolar quantum gases, Chem. Rev. **112**, 5012 (2012).

[3] J. L. Bohn, A. M. Rey, and J. Ye, Cold molecules: Progress in quantum engineering of chemistry and quantum matter, Science **357**, 1002 (2017).

[4] A. Micheli, G. K. Brennen, and P. Zoller, A toolbox for lattice-spin models with polar molecules, Nat. Phys. **2**, 341 (2006).

[5] J. Pérez-Ríos, F. Herrera, and R. V. Krems, External field control of collective spin excitations in an optical lattice of $^2\Sigma$ molecules, New J. Phys. **12**, 103007 (2010).

[6] N. Y. Yao, M. P. Zaletel, D. M. Stamper-Kurn, and A. Vishwanath, A quantum dipolar spin liquid, Nat. Phys. **14**, 405 (2018).

[7] S. L. Cornish, M. R. Tarbutt, and K. R. A. Hazzard, Quantum computation and quantum simulation with ultracold molecules, ArXiv:2401.05086 (2024).

[8] M. Hughes, M. D. Frye, R. Sawant, G. Bhole, J. A. Jones, S. L. Cornish, M. R. Tarbutt, J. M. Hutson, D. Jaksch, and J. Mur-Petit, Robust entangling gate for polar molecules using magnetic and microwave fields, Phys. Rev. A **101**, 062308 (2020).

[9] M. Karra, K. Sharma, B. Friedrich, S. Kais, and D. Herschbach, Prospects for quantum computing with an array of ultracold polar paramagnetic molecules, J. Chem. Phys. **144**, 094301 (2016).

[10] H. Son, J. J. Park, Y.-K. Lu, A. O. Jamison, T. Karman, and W. Ketterle, Control of reactive collisions by quantum interference, Science **375**, 1006 (2022).

[11] T. M. Rvachov, H. Son, A. T. Sommer, S. Ebadi, J. J. Park, M. W. Zwierlein, W. Ketterle, and A. O. Jamison, Long-lived ultracold molecules with electric and magnetic dipole moments, Phys. Rev. Lett. **119**, 143001 (2017).

[12] J. J. Park, Y.-K. Lu, A. O. Jamison, T. V. Tscherbul, and W. Ketterle, A Feshbach resonance in collisions between triplet ground-state molecules, Nature **614**, 54 (2023).

[13] T. Langen, G. Valtolina, D. Wang, and J. Ye, Quantum state manipulation and science of ultracold molecules, ArXiv:2305.13445.

[14] N. Fitch and M. Tarbutt, Chapter three - laser-cooled molecules, Adv. At., Mol. Opt. Phys. **70**, 157 (2021).

[15] G. Valtolina, K. Matsuda, W. G. Tobias, J.-R. Li, L. De Marco, and J. Ye, Dipolar evaporation of reactive molecules to below the Fermi temperature, Nature **588**, 239 (2020).

[16] M. Duda, X.-Y. Chen, A. Schindewolf, R. Bause, J. von Milczewski, R. Schmidt, I. Bloch, and X.-Y. Luo,

Transition from a polaronic condensate to a degenerate Fermi gas of heteronuclear molecules, Nat. Phys. **19**, 720 (2023).

[17] N. Bigagli, W. Yuan, S. Zhang, B. Bulatovic, T. Karman, I. Stevenson, and S. Will, Observation of Bose-Einstein condensation of dipolar molecules, ArXiv:2312.10965 (2023).

[18] C. Chin, R. Grimm, P. Julienne, and E. Tiesinga, Feshbach resonances in ultracold gases, Rev. Mod. Phys. **82**, 1225 (2010).

[19] V. Barbé, A. Ciamei, B. Pasquiou, L. Reichsöllner, F. Schreck, P. S. Żuchowski, and J. M. Hutson, Observation of Feshbach resonances between alkali and closed-shell atoms, Nat. Phys. **14**, 881 (2018).

[20] A. Green, H. Li, J. H. See Toh, X. Tang, K. C. McCormick, M. Li, E. Tiesinga, S. Kotochigova, and S. Gupta, Feshbach resonances in p-wave three-body recombination within Fermi-Fermi mixtures of open-shell ^{6}Li and closed-shell ^{173}Yb atoms, Phys. Rev. X **10**, 031037 (2020).

[21] T. Franzen, A. Guttridge, K. E. Wilson, J. Segal, M. D. Frye, J. M. Hutson, and S. L. Cornish, Observation of magnetic Feshbach resonances between Cs and ^{173}Yb, Phys. Rev. Res. **4**, 043072 (2022).

[22] M. Borkowski, L. Reichsöllner, P. Thekkeppatt, V. Barbé, T. van Roon, K. van Druten, and F. Schreck, Active stabilization of kilogauss magnetic fields to the ppm level for magnetoassociation on ultranarrow Feshbach resonances, Rev. Sci. Instrum. **94**, 073202 (2023).

[23] M. D. Frye, S. L. Cornish, and J. M. Hutson, Prospects of forming high-spin polar molecules from ultracold atoms, Phys. Rev. X **10**, 041005 (2020).

[24] E. Soave, A. Canali, Z.-X. Ye, M. Kreyer, E. Kirilov, and R. Grimm, Optically trapped Feshbach molecules of fermionic ^{161}Dy and ^{40}K, Phys. Rev. Res. **5**, 033117 (2023).

[25] R. Van Zee, C. Baumann, and W. Weltner, HCr, LiCr, and NaCr molecules: ESR and ground state properties, Chem. Phys. Lett. **113**, 524 (1985).

[26] Z. Pavlović, H. R. Sadeghpour, R. Côté, and B. O. Roos, CrRb: A molecule with large magnetic and electric dipole moments, Phys. Rev. A **81**, 052706 (2010).

[27] S. Hensler, A. Griesmaier, J. Werner, A. Görlitz, and T. Pfau, A two species trap for chromium and rubidium atoms, J. Mod. Opt. **51**, 1807 (2004).

[28] A. Ciamei, S. Finelli, A. Cosco, M. Inguscio, A. Trenkwalder, and M. Zaccanti, Double-degenerate Fermi mixtures of ^{6}Li and ^{53}Cr atoms, Phys. Rev. A **106**, 053318 (2022).

[29] A. Ciamei, S. Finelli, A. Trenkwalder, M. Inguscio, A. Simoni, and M. Zaccanti, Exploring ultracold collisions in ^{6}Li–^{53}Cr Fermi mixtures: Feshbach resonances and scattering properties of a novel alkali-transition metal system, Phys. Rev. Lett. **129**, 093402 (2022).

[30] D. S. Petrov, C. Salomon, and G. V. Shlyapnikov, Weakly bound dimers of fermionic atoms, Phys. Rev. Lett. **93**, 090404 (2004).

[31] M. Jag, M. Cetina, R. S. Lous, R. Grimm, J. Levinsen, and D. S. Petrov, Lifetime of Feshbach dimers in a Fermi-Fermi mixture of ^{6}Li and ^{40}K, Phys. Rev. A **94**, 062706 (2016).

[32] L. Vichi and S. Stringari, Collective oscillations of an interacting trapped Fermi gas, Phys. Rev. A **60**, 4734 (1999).

[33] S. D. Gensemer and D. S. Jin, Transition from collisionless to hydrodynamic behavior in an ultracold Fermi gas, Phys. Rev. Lett. **87**, 173201 (2001).

[34] G. Ferrari, M. Inguscio, W. Jastrzebski, G. Modugno, G. Roati, and A. Simoni, Collisional properties of ultracold K-Rb mixtures, Phys. Rev. Lett. **89**, 053202 (2002).

[35] F. Ferlaino, R. J. Brecha, P. Hannaford, F. Riboli, G. Roati, G. Modugno, and M. Inguscio, Dipolar oscillations in a quantum degenerate Fermi–Bose atomic mixture, J. Opt. B: Quantum Semiclassical Opt. **5**, S3 (2003).

[36] J. Li, J. Liu, L. Luo, and B. Gao, Three-body recombination near a narrow Feshbach resonance in ^{6}Li, Phys. Rev. Lett. **120**, 193402 (2018).

[37] M. Zaccanti, Mass-imbalanced Fermi mixtures with resonant interactions, ArXiv:2306.02736.

[38] C. Regal, Ph.D. thesis, University of Colorado, Boulder, 2006.

[39] T. Köhler, K. Góral, and P. S. Julienne, Production of cold molecules via magnetically tunable Feshbach resonances, Rev. Mod. Phys. **78**, 1311 (2006).

[40] K. E. Strecker, G. B. Partridge, and R. G. Hulet, Conversion of an atomic Fermi gas to a long-lived molecular Bose gas, Phys. Rev. Lett. **91**, 080406 (2003).

[41] C. A. Regal, C. Ticknor, J. L. Bohn, and D. S. Jin, Creation of ultracold molecules from a Fermi gas of atoms, Nature **424**, 47 (2003).

[42] E. Hodby, S. T. Thompson, C. A. Regal, M. Greiner, A. C. Wilson, D. S. Jin, E. A. Cornell, and C. E. Wieman, Production efficiency of ultracold Feshbach molecules in bosonic and fermionic systems, Phys. Rev. Lett. **94**, 120402 (2005).

[43] S. B. Papp and C. E. Wieman, Observation of heteronuclear Feshbach molecules from a ^{85}Rb $-^{87}$ Rb gas, Phys. Rev. Lett. **97**, 180404 (2006).

[44] A.-C. Voigt, M. Taglieber, L. Costa, T. Aoki, W. Wieser, T. W. Hänsch, and K. Dieckmann, Ultracold heteronuclear Fermi-Fermi molecules, Phys. Rev. Lett. **102**, 020405 (2009).

[45] T. D. Cumby, R. A. Shewmon, M.-G. Hu, J. D. Perreault, and D. S. Jin, Feshbach-molecule formation in a Bose-Fermi mixture, Phys. Rev. A **87**, 012703 (2013).

[46] T. Yamakoshi, S. Watanabe, C. Zhang, and C. H. Greene, Stochastic and equilibrium pictures of the ultracold Fano-Feshbach-resonance molecular conversion rate, Phys. Rev. A **87**, 053604 (2013).

[47] F. M. Spiegelhalder, A. Trenkwalder, D. Naik, G. Kerner, E. Wille, G. Hendl, F. Schreck, and R. Grimm, All-optical production of a degenerate mixture of ^{6}Li and ^{40}K and creation of heteronuclear molecules, Phys. Rev. A **81**, 043637 (2010).

[48] P. Politzer and J. S. Murray, The Hellmann-Feynman theorem: A perspective, J. Mol. Model. **24**, 266 (2018).

[49] D. S. Petrov, in *Many-Body Physics with Ultracold Gases: Lecture Notes of the Les Houches Summer School: Volume 94* (Oxford University Press, Oxford, 2012).

[50] A. Yang, S. Botsi, S. Kumar, S. B. Pal, M. M. Lam, I. Čepaitė, A. Laugharn, and K. Dieckmann, Singlet pathway to the ground state of ultracold polar molecules, Phys. Rev. Lett. **124**, 133203 (2020).

[51] S. T. Thompson, E. Hodby, and C. E. Wieman, Ultracold molecule production via a resonant oscillating magnetic field, Phys. Rev. Lett. **95**, 190404 (2005).

[52] M. Bartenstein, A. Altmeyer, S. Riedl, R. Geursen, S. Jochim, C. Chin, J. H. Denschlag, R. Grimm, A. Simoni, E. Tiesinga, C. J. Williams, and P. S. Julienne, Precise determination of ^{6}Li cold collision parameters by radio-frequency spectroscopy on weakly bound molecules, Phys. Rev. Lett. **94**, 103201 (2005).

[53] G. B. Partridge, K. E. Strecker, R. I. Kamar, M. W. Jack, and R. G. Hulet, Molecular probe of pairing in the BEC-BCS crossover, Phys. Rev. Lett. **95**, 020404 (2005).

[54] T. Mukaiyama, J. R. Abo-Shaeer, K. Xu, J. K. Chin, and W. Ketterle, Dissociation and decay of ultracold sodium molecules, Phys. Rev. Lett. **92**, 180402 (2004).

[55] A. Z. Lam, N. Bigagli, C. Warner, W. Yuan, S. Zhang, E. Tiemann, I. Stevenson, and S. Will, High phase-space density gas of NaCs Feshbach molecules, Phys. Rev. Res. **4**, L022019 (2022).

[56] The dynamic polarizabilities relevant for this work are $\alpha_{\mathrm{Li}}(532\ \mathrm{nm}) = -273$ a.u, $\alpha_{\mathrm{Li}}(1070\ \mathrm{nm}) = 270$ a.u., $\alpha_{\mathrm{Li}}(1560\ \mathrm{nm}) = 201$ a.u. for Li, and $\alpha_{\mathrm{Cr}}(532\ \mathrm{nm}) = 164$ a.u., $\alpha_{\mathrm{Cr}}(1070\ \mathrm{nm}) = 89$ a.u., $\alpha_{\mathrm{Cr}}(1560\ \mathrm{nm}) = 83$ a.u. for Cr.

[57] Dynamic polarizabilities of Feshbach LiCr are expected to be the sum of the atomic ones: $\alpha_{\mathrm{LiCr}}(532\ \mathrm{nm}) = -109$ a.u, $\alpha_{\mathrm{LiCr}}(1070\ \mathrm{nm}) = 359$ a.u., $\alpha_{\mathrm{LiCr}}(1560\ \mathrm{nm}) = 284$ a.u., of which the last two are consistent with our measurements.

[58] R. J. Bartlett and M. Musiał, Coupled-cluster theory in quantum chemistry, Rev. Mod. Phys. **79**, 291 (2007).

[59] N. B. Balabanov and K. A. Peterson, Systematically convergent basis sets for transition metals. I. All-electron correlation consistent basis sets for the 3D elements Sc–Zn, J. Chem. Phys. **123**, 064107 (2005).

[60] B. P. Prascher, D. E. Woon, K. A. Peterson, T. H. Dunning, and A. K. Wilson, Gaussian basis sets for use in correlated molecular calculations. VII. Valence, core-valence, and scalar relativistic basis sets for Li, Be, Na, and Mg, Theor. Chem. Acc. **128**, 69 (2011).

[61] M. Douglas and N. M. Kroll, Quantum electrodynamical corrections to the fine structure of helium, Ann. Phys. **82**, 89 (1974).

[62] B. A. Hess, Relativistic electronic-structure calculations employing a two-component no-pair formalism with external-field projection operators, Phys. Rev. A **33**, 3742 (1986).

[63] S. Boys and F. Bernardi, The calculation of small molecular interactions by the differences of separate total energies. Some procedures with reduced errors, Mol. Phys. **19**, 553 (1970).

[64] H.-J. Werner, *et al.*, Molpro, version 2019.2, a package of ab initio programs, see https://www.molpro.net.

[65] M. Kállay, P. R. Nagy, D. Mester, Z. Rolik, G. Samu, J. Csontos, J. Csóka, P. B. Szabó, L. Gyevi-Nagy, and B. Hégely, *et al.*, The MRCC program system: Accurate quantum chemistry from water to proteins, J. Chem. Phys. **152**, 074107 (2020).

[66] E. Tiesinga, C. J. Williams, and P. S. Julienne, Photoassociative spectroscopy of highly excited vibrational levels of alkali-metal dimers: Green-function approach for eigenvalue solvers, Phys. Rev. A **57**, 4257 (1998).

[67] B. R. Johnson, The renormalized Numerov method applied to calculating bound states of the coupled-channel Schroedinger equation, J. Chem. Phys. **69**, 4678 (1978).

[68] M. Gronowski, A. M. Koza, and M. Tomza, Ab initio properties of the NaLi molecule in the $a\,^3\Sigma^+$ electronic state, Phys. Rev. A **102**, 020801(R) (2020).

[69] K. Zaremba-Kopczy, M. Gronowski, A. Ciamei, M. Zaccanti, and M. Tomza, Ab initio electronic structure of the LiCr molecule: Prospects for the formation and precision measurements (to be published).

[70] H. Ladjimi and M. Tomza, Diatomic molecules of alkali-metal and alkaline-earth-metal atoms: Interaction potentials, dipole moments, and polarizabilities, ArXiv:2303.17527.

[71] T. S. Roussy, L. Caldwell, T. Wright, W. B. Cairncross, Y. Shagam, K. B. Ng, N. Schlossberger, S. Y. Park, A. Wang, J. Ye, and E. A. Cornell, An improved bound on the electron's electric dipole moment, Science **381**, 46 (2023).

[72] S. S. Kondov, C.-H. Lee, K. H. Leung, C. Liedl, I. Majewska, R. Moszynski, and T. Zelevinsky, Molecular lattice clock with long vibrational coherence, Nat. Phys. **15**, 1118 (2019).

[73] K. H. Leung, B. Iritani, E. Tiberi, I. Majewska, M. Borkowski, R. Moszynski, and T. Zelevinsky, Terahertz vibrational molecular clock with systematic uncertainty at the 10^{-14} level, Phys. Rev. X **13**, 011047 (2023).

[74] N. V. Vitanov, A. A. Rangelov, B. W. Shore, and K. Bergmann, Stimulated Raman adiabatic passage in physics, chemistry, and beyond, Rev. Mod. Phys. **89**, 015006 (2017).

[75] A. Gezerlis, S. Gandolfi, K. E. Schmidt, and J. Carlson, Heavy-light fermion mixtures at unitarity, Phys. Rev. Lett. **103**, 060403 (2009).

[76] J. E. Baarsma, K. B. Gubbels, and H. T. C. Stoof, Population and mass imbalance in atomic Fermi gases, Phys. Rev. A **82**, 013624 (2010).

[77] M. Pini, P. Pieri, R. Grimm, and G. C. Strinati, Beyond-mean-field description of a trapped unitary Fermi gas with mass and population imbalance, Phys. Rev. A **103**, 023314 (2021).

[78] O. I. Kartavtsev and A. V. Malykh, Low-energy three-body dynamics in binary quantum gases, J. Phys. B: At., Mol. Opt. Phys. **40**, 1429 (2007).

[79] J. Levinsen, T. G. Tiecke, J. T. M. Walraven, and D. S. Petrov, Atom-dimer scattering and long-lived trimers in fermionic mixtures, Phys. Rev. Lett. **103**, 153202 (2009).

[80] S. Endo, P. Naidon, and M. Ueda, Universal physics of 2+1 particles with non-zero angular momentum, Few-Body Syst. **51**, 207 (2011).

[81] D. Blume, Universal four-body states in heavy-light mixtures with a positive scattering length, Phys. Rev. Lett. **109**, 230404 (2012).

[82] B. Bazak and D. S. Petrov, Five-body Efimov effect and universal pentamer in fermionic mixtures, Phys. Rev. Lett. **118**, 083002 (2017).

[83] R. Liu, C. Peng, and X. Cui, Universal tetramer and pentamer bound states in two-dimensional fermionic mixtures, Phys. Rev. Lett. **129**, 073401 (2022).

[84] C. J. M. Mathy, M. M. Parish, and D. A. Huse, Trimers, molecules, and polarons in mass-imbalanced atomic Fermi gases, Phys. Rev. Lett. **106**, 166404 (2011).

[85] R. Liu, C. Peng, and X. Cui, Emergence of crystalline few-body correlations in mass-imbalanced Fermi polarons, Cell Rep. Phys. Sci. **3**, 100993 (2022).

[86] S. Endo, A. M. García-García, and P. Naidon, Universal clusters as building blocks of stable quantum matter, Phys. Rev. A **93**, 053611 (2016).

[87] R. Liu, W. Wang, and X. Cui, Quartet superfluid in two-dimensional mass-imbalanced Fermi mixtures, Phys. Rev. Lett. **131**, 193401 (2023).

[88] L. Anderegg, S. Burchesky, Y. Bao, S. S. Yu, T. Karman, E. Chae, K.-K. Ni, W. Ketterle, and J. M. Doyle, Observation of microwave shielding of ultracold molecules, Science **373**, 779 (2021).

[89] J.-R. Li, W. G. Tobias, K. Matsuda, C. Miller, G. Valtolina, L. De Marco, R. R. W. Wang, L. Lassablière, G. Quéméner, J. L. Bohn, and J. Ye, Tuning of dipolar interactions and evaporative cooling in a three-dimensional molecular quantum gas, Nat. Phys. **17**, 1144 (2021).

[90] B. Mukherjee, M. D. Frye, C. R. Le Sueur, M. R. Tarbutt, and J. M. Hutson, Shielding collisions of ultracold CaF molecules with static electric fields, Phys. Rev. Res. **5**, 033097 (2023).

[91] X.-Y. Chen, A. Schindewolf, S. Eppelt, R. Bause, M. Duda, S. Biswas, T. Karman, T. Hilker, I. Bloch, and X.-Y. Luo, Field-linked resonances of polar molecules, Nature **614**, 59 (2023).

[92] A. Mosk, S. Kraft, M. Mudrich, K. Singer, W. Wohlleben, R. Grimm, and M. Weidemüller, Mixture of ultracold lithium and cesium atoms in an optical dipole trap, Appl. Phy. B **73**, 791 (2001).